

Three-dimensional multi-scale line filter for segmentation and visualization of curvilinear structures in medical images

Yoshinobu Sato^{1*}, Shin Nakajima¹, Nobuyuki Shiraga¹, Hideki Atsumi¹,
Shigeyuki Yoshida², Thomas Koller³, Guido Gerig³ and Ron Kikinis¹

¹Surgical Planning Laboratory, Department of Radiology, Harvard Medical School and Brigham and Women's Hospital, Boston, MA 02115, USA

²Department of Radiology, Osaka University Medical School, Japan

³Communication Technology Laboratory, Image Science, ETH-Zentrum, Switzerland

Abstract

This paper describes a method for the enhancement of curvilinear structures such as vessels and bronchi in three-dimensional (3-D) medical images. A 3-D line enhancement filter is developed with the aim of discriminating line structures from other structures and recovering line structures of various widths. The 3-D line filter is based on a combination of the eigenvalues of the 3-D Hessian matrix. Multi-scale integration is formulated by taking the maximum among single-scale filter responses, and its characteristics are examined to derive criteria for the selection of parameters in the formulation. The resultant multi-scale line-filtered images provide significantly improved segmentation and visualization of curvilinear structures. The usefulness of the method is demonstrated by the segmentation and visualization of brain vessels from magnetic resonance imaging (MRI) and magnetic resonance angiography (MRA), bronchi from a chest CT, and liver vessels (portal veins) from an abdominal CT.

Keywords: 3-D image analysis, line detection, line measure, multi-scale integration, vessel enhancement

Received November 14, 1997; revised February 12, 1998; accepted February 28, 1998

1. INTRODUCTION

The human body contains various types of curvilinear structures—blood vessels, bronchial trees, bile ducts etc.—the visualization of which is crucial for planning and navigation during interventional therapy and biopsy (Kikinis *et al.*, 1996; Nakajima *et al.*, 1997), as well as for diagnostic purposes. There has been a considerable amount of work done on the enhancement and extraction of curvilinear structures from three-dimensional (3-D) medical images, most of which has focused on the extraction of a specific

anatomical structure from a specific imaging modality—for example, cerebral blood vessels from magnetic resonance angiography (MRA) images (Vandermeulen *et al.*, 1992; Du *et al.*, 1995; Lock *et al.*, 1995) and bronchial trees from lung CT images (Mori *et al.*, 1995). From the viewpoint of image analysis, however, the problems involved in extracting various types of curvilinear structures from 3-D images are specific enough to be treated as the same class of problem. While the study of two-dimensional (2-D) line extraction and its applications has a long history (Rosenfeld and Thurston, 1971; Vandarbrug, 1975; Fischler *et al.*, 1981; Haralick *et al.*, 1983; Gauch and Pizer, 1993; Koller *et al.*, 1995; Lindeberg, 1996), 3-D extensions of the developed methods have not been emphasized; although a recent study (Koller *et al.*, 1995; Lorenz *et al.*, 1997; Sato *et al.*, 1997b) did take account of such a 3-D extension, the investigation in the 3-D domain was quite insufficient in terms of both the consideration of

*Corresponding author. Yoshinobu Sato is with the Division of Functional Diagnostic Imaging, Biomedical Research Center, Osaka University Medical School, Suita, Osaka 565-0871, Japan. The work described in this paper was conducted while he was a visiting researcher at the Surgical Planning Laboratory, Department of Radiology, Harvard Medical School and Brigham and Women's Hospital.
(e-mail: yoshi@image.med.osaka-u.ac.jp)

the filter design and the experimental demonstration of its usefulness.

From the clinical point of view, digital subtraction angiography (DSA), which subtracts X-ray images without contrast material from X-ray angiograms, is currently regarded as the most reliable and accurate method of vascular imaging. However, MRA (Dumoulin *et al.*, 1989; Edelman *et al.*, 1990; Prince *et al.*, 1993) is seen as a potential alternative to DSA. CT angiography and conventional magnetic resonance imaging (MRI) can also be used for vascular imaging. Such 3-D imaging techniques are less invasive and provide 3-D information of the vascular structures directly, while the image quality for vessel visualization is still insufficient compared to that obtainable with DSA, especially on the visibility of small vessels and the accurate depiction of morphological information of stenoses and aneurysms.

There is a strong need for a means of imaging vascular and other curvilinear anatomical structures with 3-D information and good image quality. These two requirements are especially crucial in the planning for and navigation during interventional therapy and biopsy (Kikinis *et al.*, 1996; Nakajima *et al.*, 1997), in which the recovery of 3-D information is essential and the recovered structures should be as detailed as possible—not only because the curvilinear structures are themselves critical, but also because they are used as a ‘road map’ or landmarks for both planning and navigation. One method of acquiring images of the desired type is to use stereo reconstruction from X-ray angiograms with multiple viewpoints in order to add 3-D information (Kitamura *et al.*, 1989; Roug   *et al.*, 1994). However, stereo reconstruction is known to be a difficult technique that often involves complex manual operations. An alternative approach is to employ 3-D imaging techniques that have recently become commonly available; thin-slice MRI and helical CT scanners, for instance, are now often used in routine examinations. Our aim is to fulfill the 3-D and image-quality requirements by means of a filtering method that will both enhance and discriminate curvilinear structures in 3-D images acquired from these scanners.

In this paper, we describe a practical and general-purpose approach to 3-D line enhancement filtering. We endeavor to design a filter that is able to accomplish the following:

- (i) recovery of line structures of various widths (especially thin structures);
- (ii) removal of the effects of structures other than line structures;
- (iii) removal of the effects of nonuniformity of contrast material; and
- (iv) removal of noise and artifacts.

In order to enhance line structures of various widths, multi-scale integration of the filter responses is essential. We give consideration to determining the sampling interval of each scale. We also address practical aspects, such as sinc interpolation before line-filtering to make each voxel isotropic. Through evaluations using different imaging modalities and anatomical structures, we demonstrate the utility of the multi-scale line filter in improving the quality of the segmentation and visualization.

The paper is organized as follows. In Section 2, we derive a generalized measure of similarity to the 3-D line structure based on the eigenvalues of the Hessian matrix, and show simulation experiments using mathematical line models. In Section 3, we analyze the multi-scale integration of filter responses at discrete scales. In Section 4, we refer to several aspects of the implementation of the method. In Section 5, we give experimental results for brain vessel segmentation and visualization from MRA and MRI, bronchus segmentation from a chest CT and liver vessel segmentation from an abdominal CT. In Section 6, we discuss the work and indicate the directions of future research.

2. 3-D LINE FILTER BASED ON HESSIAN MATRIX

2.1. A generalized measure of similarity to line

The second derivative has typically been used for line enhancement filtering. The Gaussian convolution is combined with the second derivative in order to tune the filter response to the specific widths of lines as well as to reduce the effect of noise. In the one-dimensional (1-D) case, the response of the line filter is given by

$$R(x; \sigma_f) = \left\{ -\frac{d^2}{dx^2} G(x; \sigma_f) \right\} * I(x), \quad (1)$$

where $*$ denotes the convolution, $I(x)$ is an input profile function, and $G(x; \sigma_f)$ is the Gaussian function with the standard deviation σ_f defined as $(1/\sqrt{2\pi}\sigma_f) \exp(-x^2/2\sigma_f^2)$. The sign of the Gaussian derivative has been inverted so that the responses have positive values for a bright line. We consider a profile having the Gaussian shape given by

$$L(x; \sigma_x) = \exp\left(-\frac{x^2}{2\sigma_x^2}\right), \quad (2)$$

where σ_x is the standard deviation of the profile. The height of the profile is constant for any σ_x . Let the filter response to $L(x; \sigma_x)$ be $R_L(x; \sigma_f, \sigma_x)$, that is,

$$R_L(x; \sigma_x, \sigma_f) = \left\{ -\frac{d^2}{dx^2} G(x; \sigma_f) \right\} * L(x; \sigma_x). \quad (3)$$

$R_L(x; \sigma_x, \sigma_f)$ is maximum at $\sigma_x = \sigma_f/\sqrt{2}$ and $x = 0$ when σ_f is fixed. The filter with standard deviation σ_f is considered to be tuned to the Gaussian profile with $\sigma_x = \sigma_f/\sqrt{2}$. The above discussion can also be applied to other line-like profiles such as a box shape.

The 1-D line filter can be extended to multi-dimensional line filters using the Hessian matrix, which describes the second-order structures of local intensity variations around each point of a multi-dimensional image (Haralick *et al.*, 1983; Koller *et al.*, 1995; Lorenz *et al.*, 1997; Sato *et al.*, 1997b,c, 1998). The Hessian matrix of a 3-D image $I(\mathbf{x})$ (where $\mathbf{x} = (x, y, z)$) is given by

$$\nabla^2 I(\mathbf{x}) = \begin{bmatrix} I_{xx}(\mathbf{x}) & I_{xy}(\mathbf{x}) & I_{xz}(\mathbf{x}) \\ I_{yx}(\mathbf{x}) & I_{yy}(\mathbf{x}) & I_{yz}(\mathbf{x}) \\ I_{zx}(\mathbf{x}) & I_{zy}(\mathbf{x}) & I_{zz}(\mathbf{x}) \end{bmatrix}, \quad (4)$$

where partial second derivatives of the image $I(\mathbf{x})$ are represented by expressions like $I_{xx}(\mathbf{x}) = \frac{\partial^2}{\partial x^2} I(\mathbf{x})$, $I_{yz}(\mathbf{x}) = \frac{\partial^2}{\partial y \partial z} I(\mathbf{x})$, and so on.

Let the eigenvalues of $\nabla^2 I(\mathbf{x})$ be $\lambda_1(\mathbf{x})$, $\lambda_2(\mathbf{x})$ and $\lambda_3(\mathbf{x})$ ($\lambda_1(\mathbf{x}) > \lambda_2(\mathbf{x}) > \lambda_3(\mathbf{x})$), and their corresponding eigenvectors be $\mathbf{e}_1(\mathbf{x})$, $\mathbf{e}_2(\mathbf{x})$ and $\mathbf{e}_3(\mathbf{x})$ respectively. The eigenvector $\mathbf{e}_1(\mathbf{x})$, corresponding to the largest eigenvalue $\lambda_1(\mathbf{x})$, represents the direction along which the second derivative is maximum, and $\lambda_1(\mathbf{x})$ gives the maximum second derivative value. The partial second derivatives of $I(\mathbf{x})$ in Equation (4) can be replaced by the partial second derivatives of Gaussian, for example,

$$I_{xx}(\mathbf{x}; \sigma_f) = \left\{ \frac{\partial^2}{\partial x^2} G(\mathbf{x}; \sigma_f) \right\} * I(\mathbf{x}), \quad (5)$$

where $G(\mathbf{x}; \sigma_f)$ is an isotropic Gaussian function with standard deviation σ_f . Using the Hessian matrix $\nabla^2 I(\mathbf{x}; \sigma_f)$ based on the second derivatives of Gaussian with σ_f , the eigenvalues $\lambda_1(\mathbf{x}; \sigma_f)$, $\lambda_2(\mathbf{x}; \sigma_f)$ and $\lambda_3(\mathbf{x}; \sigma_f)$ as filter responses can be tuned to a specific width of 3-D line.

Let us consider an ideal bright 3-D line image with Gaussian cross-sectional images given by

$$L(\mathbf{x}; \sigma_r) = \exp\left(-\frac{x^2 + y^2}{2\sigma_r^2}\right), \quad (6)$$

where σ_r is the standard deviation that controls the width of the line, and the height is constant for any σ_r . Let $\nabla^2 L(\mathbf{x}; \sigma_r, \sigma_f)$ be the Hessian matrix combined with the Gaussian convolution with σ_f for the ideal line $L(\mathbf{x}; \sigma_r)$. Among the eigenvalues of $\nabla^2 L(\mathbf{x}; \sigma_r, \sigma_f)$, both λ_2 and λ_3 have the same minimum at $x = y = 0$ (the center of the line) and $\sigma_r = \sigma_f$ when σ_f is fixed. When λ_2 and λ_3 are minimum, λ_1 is

zero. Therefore, the conditions of a bright line can be regarded as

$$\lambda_1 \approx 0 \quad \text{and} \quad \lambda_2 \approx \lambda_3 \ll 0. \quad (7)$$

Based on the condition $\lambda_2 \approx \lambda_3 \ll 0$, the following has been suggested as similarity measures to a line structure (Koller *et al.*, 1995; Sato *et al.*, 1997b):

$$\lambda_{\min_{23}} = \begin{cases} \min(-\lambda_2, -\lambda_3) = -\lambda_2, & \lambda_3 < \lambda_2 < 0 \\ 0, & \text{otherwise} \end{cases} \quad (8)$$

and

$$\lambda_{g\text{-mean}_{23}} = \begin{cases} \sqrt{\lambda_2 \lambda_3}, & \lambda_3 < \lambda_2 < 0 \\ 0, & \text{otherwise.} \end{cases} \quad (9)$$

For the cases $\lambda_2 \leq 0$ and $\lambda_3 \leq 0$, $\lambda_{\min_{23}}$ can be rewritten as

$$\lambda_{\min_{23}} = -\lambda_2 = |\lambda_3| \left(\frac{\lambda_2}{\lambda_3} \right), \quad (10)$$

and $\lambda_{g\text{-mean}_{23}}$ as

$$\lambda_{g\text{-mean}_{23}} = \sqrt{\lambda_2 \lambda_3} = |\lambda_3| \left(\frac{\lambda_2}{\lambda_3} \right)^{0.5}. \quad (11)$$

Now, we generalize these two measures and introduce a new measure defined as

$$\lambda_{23} = \begin{cases} |\lambda_3| w_{23}(\lambda_2; \lambda_3), & \lambda_3 < \lambda_2 < 0 \\ 0, & \text{otherwise,} \end{cases} \quad (12)$$

in which

$$w_{23}(\lambda_2; \lambda_3) = \left(\frac{\lambda_2}{\lambda_3} \right)^{\gamma_{23}}, \quad (13)$$

where γ_{23} ($\gamma_{23} \geq 0$) controls the sharpness of the selectivity for the cross-section isotropy. In the definition of λ_{23} , $|\lambda_3|$ is multiplied by the weight function $w_{23}(\lambda_2; \lambda_3)$ which decreases with the deviation from the condition $\lambda_3 = \lambda_2$. λ_{23} is equivalent to $\lambda_{\min_{23}}$ and $\lambda_{g\text{-mean}_{23}}$ when $\gamma_{23} = 1$ and $\gamma_{23} = 0.5$ respectively (Figure 1a). When $|\lambda_3| \gg |\lambda_2| \approx 0$, the structure should be regarded as sheet-like rather than line-like and λ_{23} should not be large. It is important to be able to discriminate line structures from sheet-like structures because 3-D medical images often contain strong sheet-like structures such as the skin or the skull.

The condition $\lambda_1 \approx 0$ should be combined with the similarity measure to a line. As in the definition of λ_{23} , we introduce a weight function that decreases with the deviation from the condition $\lambda_1 = 0$. The line measure is defined as

$$\lambda_{123} = \begin{cases} \lambda_{23} w_{12}(\lambda_1; \lambda_2), & \lambda_3 < \lambda_2 < 0 \\ 0, & \text{otherwise,} \end{cases} \quad (14)$$

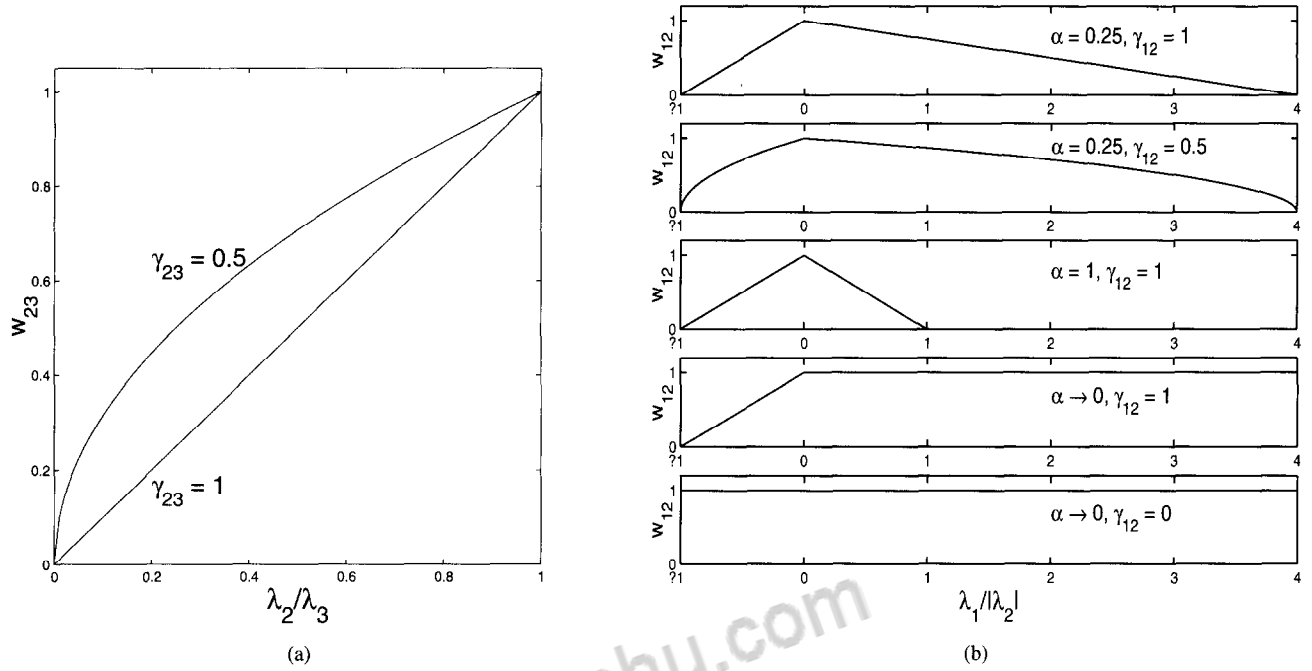


Figure 1. Weight functions in the similarity measure to a line, λ_{123} . (a) $w_{23}(\lambda_2; \lambda_3)$ with different values of γ_{23} . (b) $w_{12}(\lambda_1; \lambda_3)$ with different values of γ_{12} and α .

in which $w_{12}(\lambda_1; \lambda_2)$ is a weight function written as

$$w_{12}(\lambda_1; \lambda_2) = \begin{cases} \left(1 + \frac{\lambda_1}{|\lambda_2|}\right)^{\gamma_{12}}, & \lambda_1 \leq 0 \\ \left(1 - \alpha \frac{\lambda_1}{|\lambda_2|}\right)^{\gamma_{12}}, & \frac{|\lambda_2|}{\alpha} > \lambda_1 > 0 \\ 0, & \text{otherwise,} \end{cases} \quad (15)$$

where $\gamma_{12} \geq 0$ and $0 < \alpha \leq 1.0$. α is introduced in order to give $w_{12}(\lambda_1; \lambda_2)$ an asymmetrical characteristic in the negative and the positive regions of λ_1 (Figure 1b). When λ_1 is negative and $|\lambda_1| \approx |\lambda_2| \gg 0$, the structure should be regarded as blob-like rather than line-like. Because noise components typically have blob-like shapes, it is important that the system possesses the ability to discriminate between lines and blobs. Thus, for negative λ_1 , the weight function should decrease with deviation from $\lambda_1 = 0$ in the same manner as in the case of the discrimination between sheets and lines. When λ_1 is positive, the structure involves concavity in the estimated line direction. The effects of α are shown in simulation experiments of the next subsection.

In summary, we have derived a generalized measure of similarity to a line, $\lambda_{123}(x; \sigma_f)$. Substituting Equation (13) for $w_{23}(\lambda_2; \lambda_3)$ in Equation (12) and further substituting

Equations (12) and (15) for λ_{23} and $w_{12}(\lambda_1; \lambda_2)$ in Equation (14) respectively, we have

$$\lambda_{123} = \begin{cases} |\lambda_3| \left(\frac{\lambda_2}{\lambda_3}\right)^{\gamma_{23}} \left(1 + \frac{\lambda_1}{|\lambda_2|}\right)^{\gamma_{12}}, & \lambda_3 < \lambda_2 < \lambda_1 \leq 0 \\ |\lambda_3| \left(\frac{\lambda_2}{\lambda_3}\right)^{\gamma_{23}} \left(1 - \alpha \frac{\lambda_1}{|\lambda_2|}\right)^{\gamma_{12}}, & \lambda_3 < \lambda_2 < 0 < \lambda_1 < \frac{|\lambda_2|}{\alpha} \\ 0, & \text{otherwise.} \end{cases} \quad (16)$$

When $\gamma_{23} = \gamma_{12} = 1$, we have

$$\lambda_{123} = \begin{cases} |\lambda_2| + \lambda_1, & \lambda_3 < \lambda_2 < \lambda_1 \leq 0 \\ |\lambda_2| - \alpha \lambda_1, & \lambda_3 < \lambda_2 < 0 < \lambda_1 < \frac{|\lambda_2|}{\alpha} \\ 0, & \text{otherwise.} \end{cases} \quad (17)$$

When $\gamma_{23} = \gamma_{12} = 0.5$, we have

$$\lambda_{123} = \begin{cases} \sqrt{|\lambda_3|(|\lambda_2| + \lambda_1)}, & \lambda_3 < \lambda_2 < \lambda_1 \leq 0 \\ \sqrt{|\lambda_3|(|\lambda_2| - \alpha \lambda_1)}, & \lambda_3 < \lambda_2 < 0 < \lambda_1 < \frac{|\lambda_2|}{\alpha} \\ 0, & \text{otherwise.} \end{cases} \quad (18)$$

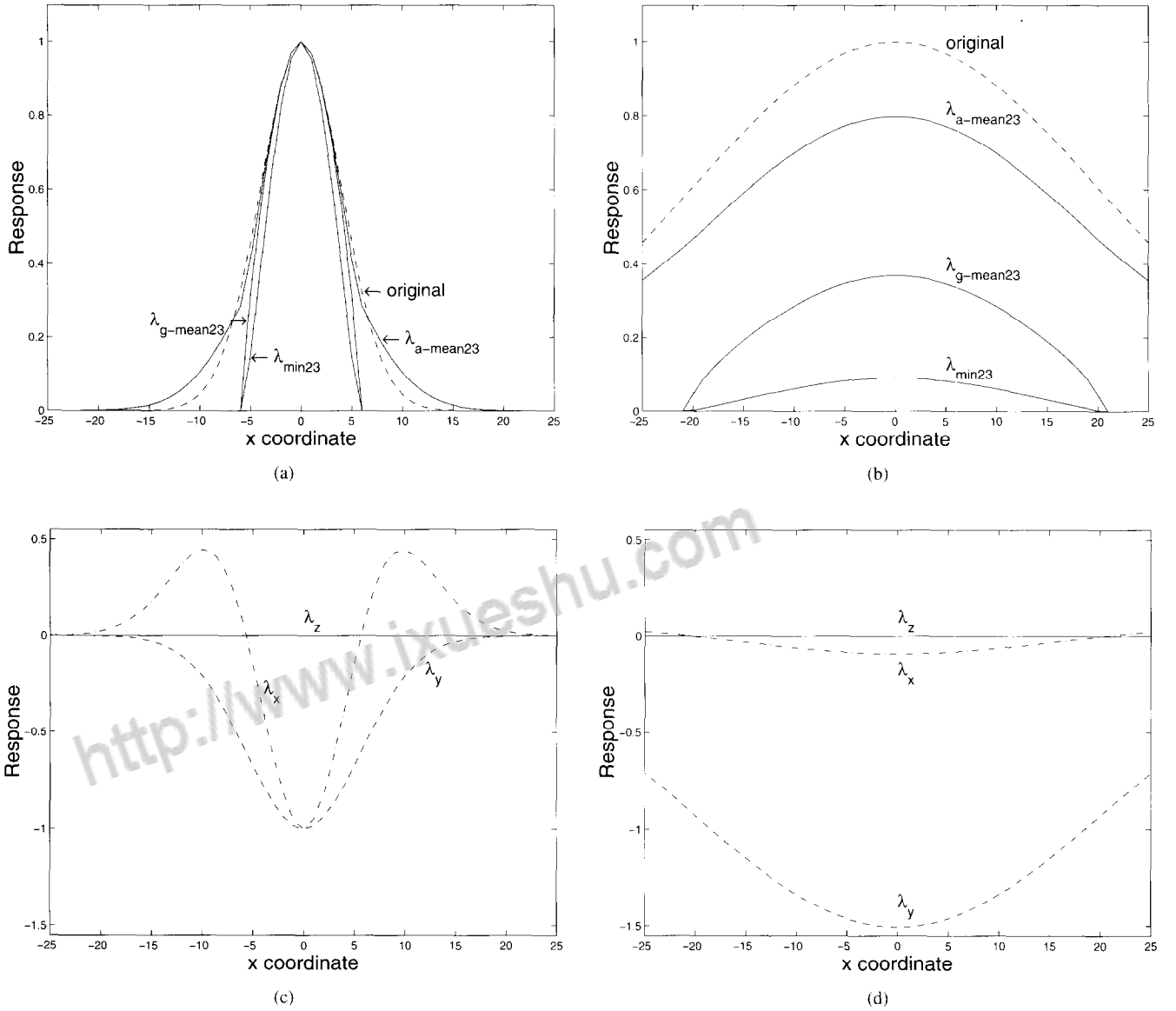


Figure 2. Responses of eigenvalues and 3-D line filters to $L_{\text{elliptic}}(\mathbf{x}; \sigma_x, \sigma_y)$ along the x -axis. The eigenvalues and filter responses are normalized so that $|\lambda_2|$ and $|\lambda_3|$ are one at $x = y = 0$ when $\sigma_x = \sigma_y = \sigma_f = 4$. (a) $\lambda_{g-mean23}$, $\lambda_{a-mean23}$, λ_{min23} , and the original profile for the ideal line case ($\sigma_x = \sigma_y = 4$ in $L_{\text{elliptic}}(\mathbf{x}; \sigma_x, \sigma_y)$, $\sigma_f = 4$). (b) $\lambda_{g-mean23}$, $\lambda_{a-mean23}$, λ_{min23} , and the original profile for the sheet-like case ($\sigma_x = 20$ and $\sigma_y = 3$ in $L_{\text{elliptic}}(\mathbf{x}; \sigma_x, \sigma_y)$, $\sigma_f = 4$). (c) Eigenvalues for the ideal line case. (d) Eigenvalues for the sheet-like case.

2.2. Simulation using mathematical line models

The generalized line measure has been introduced based on the ideal line with an isotropic Gaussian cross section. To examine the effects of parameters γ_{23} , γ_{12} and α involved in the generalized line measure, we perform simulation experiments using synthesized images, which model lines with an elliptic cross section, curved lines and branches.

2.2.1. Line model with elliptic cross section

Our line measure generalizes λ_{min23} in Equation (8) and $\lambda_{g-mean23}$ in Equation (9). An alternative measure is to use the arithmetic mean of $-\lambda_2$ and $-\lambda_3$, which is given by

$$\lambda_{a-mean23} = -\frac{\lambda_2 + \lambda_3}{2}. \quad (19)$$

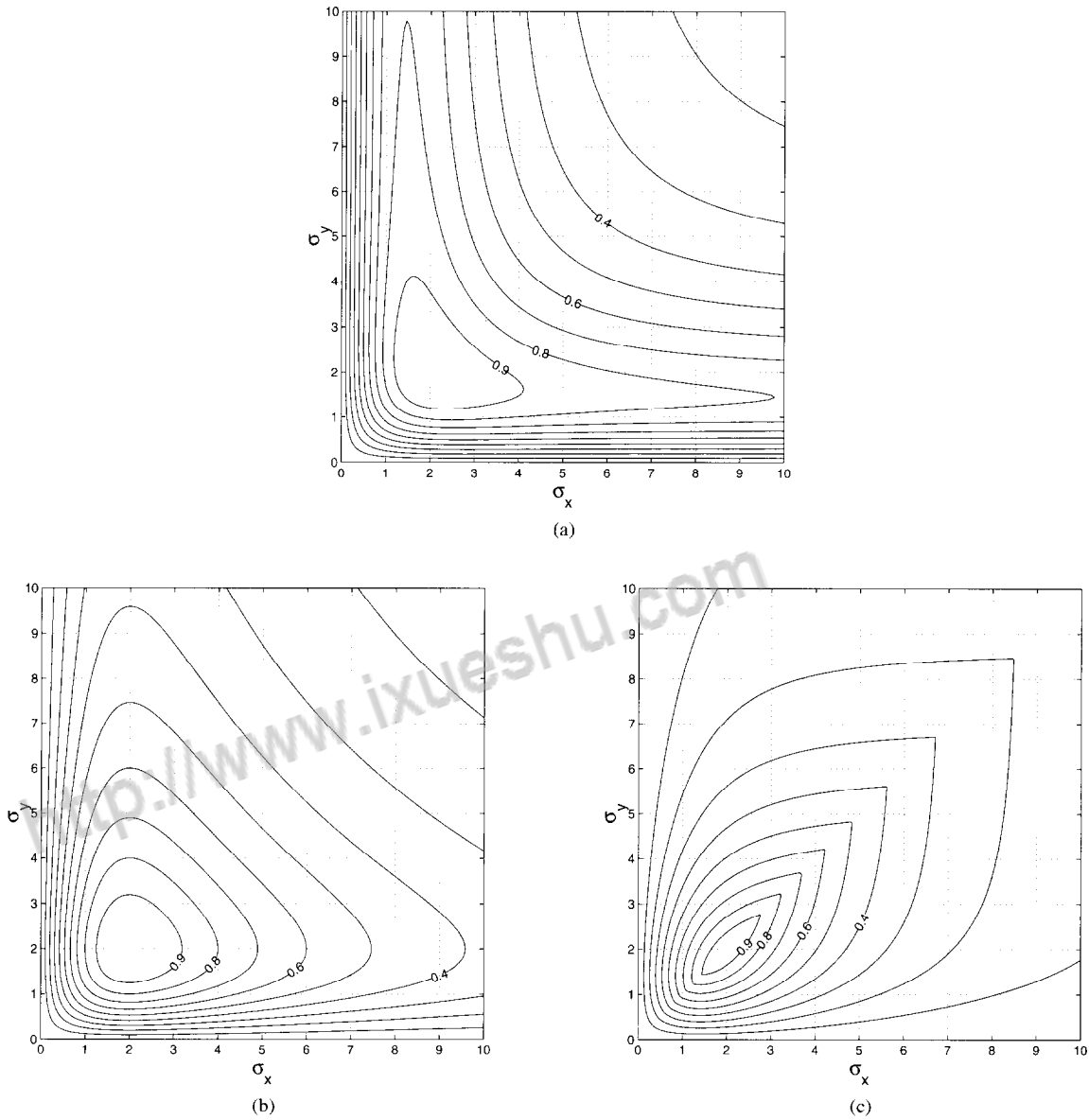


Figure 3. Responses of 3-D line filters to $L_{\text{elliptic}}(\mathbf{x}; \sigma_x, \sigma_y)$ at $x = y = 0$ with variable σ_x and σ_y at the center of the line. The responses are normalized so that $|\lambda_2|$ and $|\lambda_3|$ are one at $x = y = 0$ when $\sigma_x = \sigma_y = \sigma_f = 2$. (a) $\lambda_{a\text{-mean}23}$, (b) $\lambda_{g\text{-mean}23}$, (c) $\lambda_{\min23}$.

To compare these three measures, let us consider a 3-D line image with elliptic (non-isotropic Gaussian) cross-sections given by

$$L_{\text{elliptic}}(\mathbf{x}; \sigma_x, \sigma_y) = \exp\left\{-\left(\frac{x^2}{2\sigma_x^2} + \frac{y^2}{2\sigma_y^2}\right)\right\}. \quad (20)$$

When $\sigma_x = \sigma_y$, $L_{\text{elliptic}}(\mathbf{x}; \sigma_x, \sigma_y)$ can be regarded as an ideal line. Figure 2 shows the plots of the three measures and the

eigenvalue variations of the Hessian matrix along the x -axis for the ideal line [$\sigma_x = \sigma_y = 4$ in Equation (20), $\sigma_f = 4$] and the sheet-like ($\sigma_x = 20$, $\sigma_y = 3$, $\sigma_f = 4$) cases. The directions of the three eigenvectors at the points on the x -axis are identical to the x , y and z axes in the 3-D images modeled by Equation (20). Let \mathbf{e}_x , \mathbf{e}_y and \mathbf{e}_z be eigenvectors whose directions are identical to the x , y , and z axes respectively, and let λ_x , λ_y and λ_z be the respective corresponding eigenvalues.

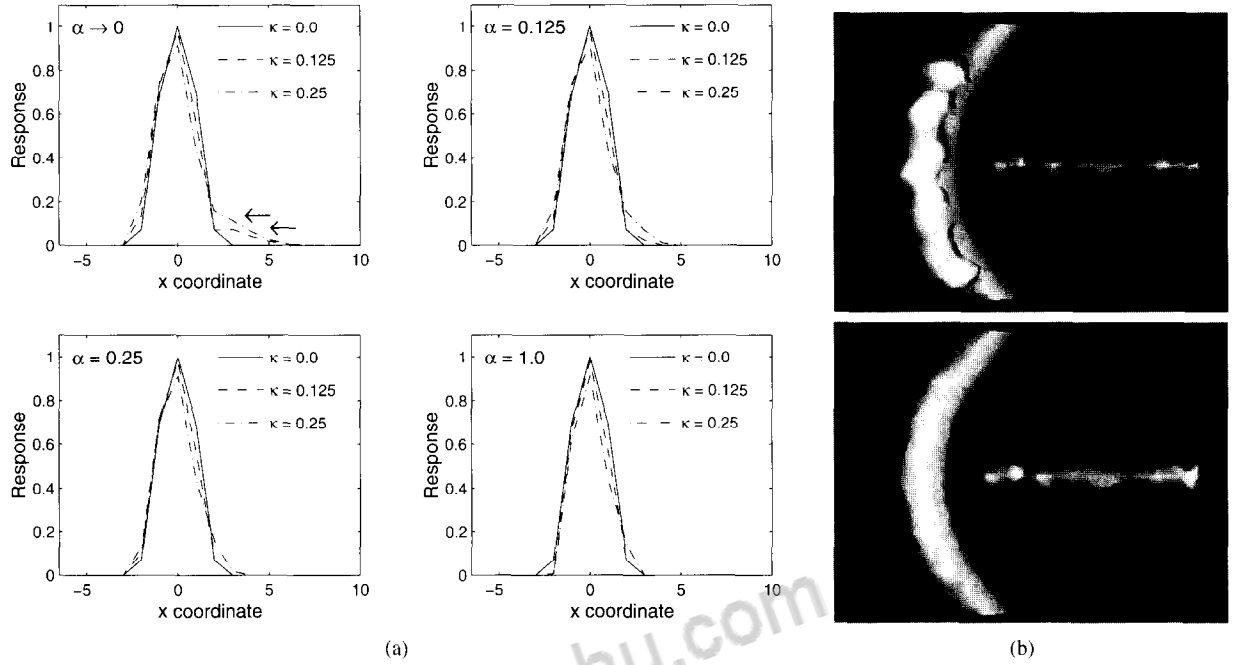


Figure 4. Simulation using the curved line model. (a) Profiles of line-filtered images of curved line model with $\sigma_r = 1.5$ and three different κ values (see Appendix A.1) when $\sigma_f = 1.5$ and $\gamma_{23} = \gamma_{12} = 1$. Upper left, $\alpha \rightarrow 0.0$. The filter gives higher response at lower slopes of the profiles (indicated by arrows). Upper right, $\alpha = 0.125$; lower left, $\alpha = 0.25$; lower right, $\alpha = 1$. (b) Simulation results using synthesized images including a high-intensity curved line and a low-intensity straight line with additive Gaussian noise (see Appendix A.2) when $\gamma_{23} = \gamma_{12} = 1$. Upper, $\alpha \rightarrow 0.0$. Spurious bump components are attached on the opposite side of the center of curvature. Lower, $\alpha = 0.25$.

Figure 2a and b shows the plots of $\lambda_{g\text{-mean}_{23}}$, $\lambda_{a\text{-mean}_{23}}$, and $\lambda_{\min_{23}}$ as well as the original profiles, while Figure 2c and d shows the plots of λ_x , λ_y and λ_z . In the ideal line case, both λ_2 and λ_3 are negative with large absolute values near the line centers. Since λ_3 tends to have a larger absolute value in the sheet-like case than in the line case (Figure 2d), $\lambda_{a\text{-mean}_{23}}$ still gives a high response in the sheet-like case even if λ_2 has a small absolute value. Figure 3 shows the responses of the three measures at the center of the line ($x = y = 0$) when σ_x and σ_y in Equation (20) are varied. While $\lambda_{\min_{23}}$ and $\lambda_{g\text{-mean}_{23}}$ decrease with deviations from the conditions $\sigma_x \approx \sigma_f$ and $\sigma_y \approx \sigma_f$, $\lambda_{a\text{-mean}_{23}}$ gives high responses if $\sigma_x \approx \sigma_f/\sqrt{2}$ or $\sigma_y \approx \sigma_f/\sqrt{2}$. Thus, $\lambda_{a\text{-mean}_{23}}$ gives relatively high responses to sheet-like structures while $\lambda_{\min_{23}}$ [$\gamma_{23} = 1$ in Equation (13)] and $\lambda_{g\text{-mean}_{23}}$ [$\gamma_{23} = 0.5$ in Equation (13)] are able to discriminate line structures from sheet-like structures.

2.2.2. Curved line model

We consider the effect of a curved axis. While the responses of our line measure to $L_{\text{elliptic}}(\mathbf{x}; \sigma_x, \sigma_y)$ in Equation (20) are independent of $w_{12}(\lambda_1; \lambda_2)$, its influence cannot be ignored especially when the line axis has high curvature.

Let r be the radius of curvature of the curved line axis, and σ_r be the standard deviation of isotropic Gaussian cross sections (see Appendix A.1 for the detailed descriptions of the curved line model). We define the normalized curvature κ as $\kappa = \sigma_r/r$. Figure 4a shows the plots of filter responses to the curved lines with three values of κ . Four different values of α in $w_{12}(\lambda_1; \lambda_2)$ were used, while γ_{23} and γ_{12} were fixed ($\gamma_{23} = \gamma_{12} = 1$). These plots show the profiles along the straight line orthogonal to the curved line axis and passing through the center of curvature at $x = -r = -\sigma_r/\kappa$ ($\sigma_r = 1.5$ was used). When $\alpha = 0$, the filter gives a higher response (indicated by arrows in the upper left-hand frame of Figure 4a) at lower slopes of the profiles on the opposite side of the center of curvature with κ increasing.

To perceive typical situations where the response at lower slopes causes undesirable effects, we consider a 3-D image including a curved line with high intensity and a line with low intensity. In the velocity magnitude images obtained using phase-contrast MRA (Dumoulin *et al.*, 1989), the signal levels of vessels widely spread from low to high intensity because of the wide variations of the blood flow velocity. Figure 4b shows the simulation results for the synthesized image

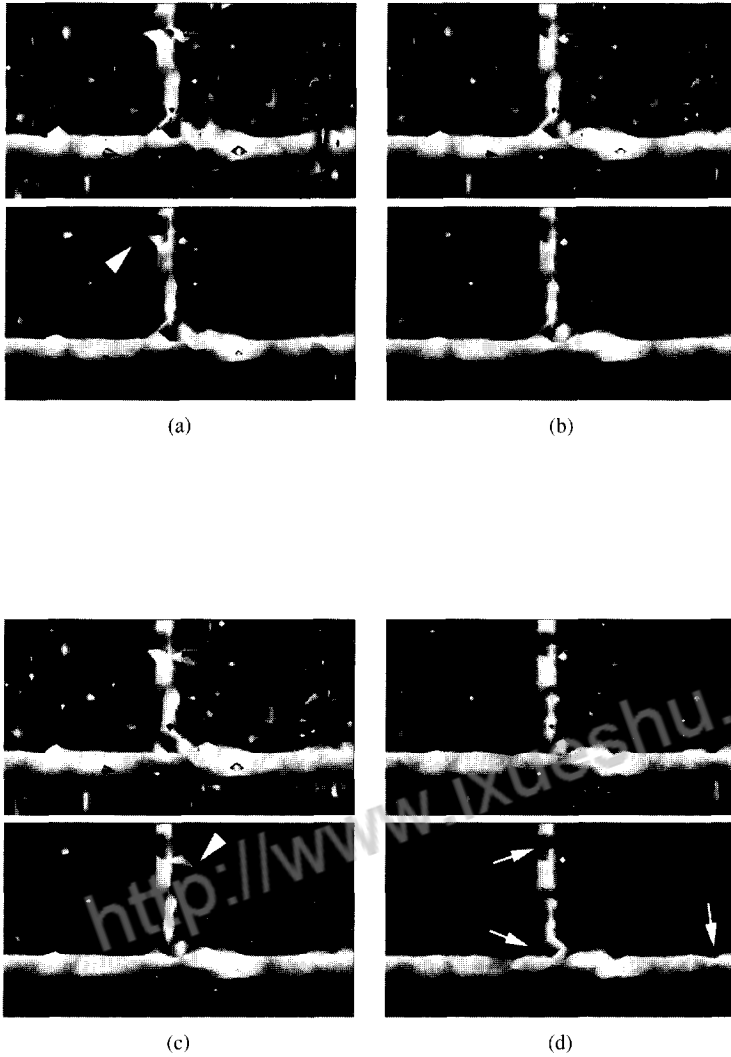


Figure 5. Simulation using the branch model. (a)–(d) Iso-surface visualization (surface rendering) of the responses of 3-D line filters with different shapes of $w_{12}(\lambda_1; \lambda_2)$ to the branch model (see Appendix A.3). The threshold values are 0.25 in the left-hand frame and 0.3 in the right-hand frame, assuming that the responses are normalized so that $|\lambda_2|$ and $|\lambda_3|$ are one at $x = y = 0$ for the ideal straight line. (a) $\gamma_{12} = 1.0$ and $\alpha \rightarrow 0$. A spurious branch can be seen (shown by an arrowhead). (b) $\gamma_{12} = 1.0$ and $\alpha = 0.25$. (c) $\gamma_{12} = 0.5$ and $\alpha = 0.25$. A spurious branch can be seen (shown by an arrowhead). (d) $\gamma_{12} = 1.0$ and $\alpha = 1$. The main line structure is easily fragmented (shown by arrows). (e) Minimum response values at which the branch is fragmented into two connected components for the synthesized branch model without noise when α is varied.

modeling such a situation. The synthesized image includes a high-intensity curved line and low-intensity straight line with additive Gaussian noise (see Appendix A.2 for details). The iso-surfaces of each line-filtered 3-D image are shown using the line measures with two different values of α and $\gamma_{23} = \gamma_{12} = 1$. When $\alpha = 0$, spurious bump components are attached on the opposite side of the center of curvature while the extraction of the low-intensity line is incomplete

(Figure 4b, upper frame). When $\alpha = 0.25$, not only these unwanted components are reduced but also the low-intensity line is extracted better (Figure 4b, lower frame).

2.2.3. Branch model

The effect of branches is another important issue. Figure 5 shows the simulation results for the synthesized image modeling a branch with additive Gaussian noise (see Appendix A.3

for the details of the model). The two iso-surfaces for each line-filtered 3-D image are shown using the line measures with four different shapes of $w_{12}(\lambda_1; \lambda_2)$. Spurious branch structures originating from noise are seen to be connected to the line structure in Figure 5a ($\gamma_{12} = 1, \alpha = 0$) and c ($\gamma_{12} = 0.5, \alpha = 0.25$). The spurious branches can significantly affect the results of segmentation based on thresholding and connectivity analysis, which is a typical procedure for extracting 3-D line structures, although separated noise components can be removed to some extent by connectivity analysis. In Figure 5d ($\gamma_{12} = 1, \alpha = 1.0$), the main line structure is easy to be fragmented. There is thus a trade-off between maximizing the preservation of true branches and minimizing noise and the spurious branch detection. As a typical undesirable effect at a branch, a spurious hole is observed at the center of the branch. When $\gamma_{12} = 0.5$ (Figure 5c), this spurious hole becomes smaller than when $\gamma_{12} = 1$.

The trade-off can be understood by observing Figure 2c which shows the basic relations of eigenvalues for the ideal line. In our line measure, the eigenvector with the maximum eigenvalue is selected as the line direction. While λ_z is maximum in the central regions of the line model in Figure 2c, λ_x is maximum in the surrounding regions. In the surrounding regions, the selected line direction e_x is the radial direction from the center of the line. Thus, the reduction of the response with the value of λ_1 being large (that is, decreasing γ_{12} and increasing α) avoids attaching spurious branches to main line structures. However, suppression of spurious branches also leads to easier fragmentation of true branches.

Figure 5e plots the minimum response values at which the branch is fragmented into two connected components for the synthesized branch model without noise (see Appendix A.3) when α is varied. The plots are shown when $\gamma_{12} = 1$ and $\gamma_{12} = 0.5$. γ_{23} and α need to be adjusted to obtain a good compromise of the trade-off. Especially when $\gamma_{12} = \gamma_{23} = 1$, the minimum response of branch fragmentation is almost constant in the range of $0 \leq \alpha \leq 0.25$. Thus, in this particular case, $\alpha = 0.25$ optimizes the trade-off.

3. MULTI-SCALE INTEGRATION OF FILTER RESPONSES

3.1. Integration of continuous scales

Filter responses tuned to different line widths can be combined in order to recover line structures of various widths. One method of integrating multi-scale responses, which has been applied successfully to 2-D line detection (Koller *et al.*, 1995; Sato *et al.*, 1997a), is to normalize the filter responses of each scale (Lindeberg, 1996) and then select the maximum response among the multiple scales. In the 1-D case, the filter response using the normalized second derivative of Gaussian

is given by

$$R(x; \sigma_f) = \sigma_f^2 \left\{ -\frac{d^2}{dx^2} G(x; \sigma_f) \right\} * I(x), \quad (21)$$

which is designed to give the same magnitude of response at the optimal scales for the line profiles $L(x; \sigma_x)$ in Equation (2). Similarly, in the 3-D case, the normalized filter response is given by

$$R(\mathbf{x}; \sigma_f) = \sigma_f^2 \lambda_{123}(\mathbf{x}; \sigma_f). \quad (22)$$

The multi-scale integration of the filter responses is defined by

$$M(\mathbf{x}) = \max_{\sigma_f} R(\mathbf{x}; \sigma_f). \quad (23)$$

In order to analyze multi-scale filter responses and develop design criteria for the multi-scale integration, we observe the variations in the height and width of the original line image $L(\mathbf{x}; \sigma_r)$ in Equation (6) and its filter responses. The multi-scale response for $L(\mathbf{x}; \sigma_r)$ is given by

$$M_L(\mathbf{x}; \sigma_r) = \max_{\sigma_f} R_L(\mathbf{x}; \sigma_r, \sigma_f). \quad (24)$$

We define the height measure of the multi-scale filter response as $h_M(\sigma_r) = M_L(0, 0, z; \sigma_r)$. Since the filter response is normalized, $h_M(\sigma_r)$ is constant regardless of σ_r ; that is,

$$h_M(\sigma_r) = h_{M_c}, \quad (25)$$

where $h_{M_c} = 0.25$ (see Appendix B for the derivation of $h_{M_c} = 0.25$). We define the width measure $w_M(\sigma_r)$ of the multi-scale filter response as the distance $\sqrt{x_0^2 + y_0^2}$ from the z -axis to the circular locus where $M_L(x_0, y_0, z; \sigma_r)$ gives half of the maximum response, that is, $h_{M_c}/2$. Let $w'_M(\sigma_r)$ be the ratio of $w_M(\sigma_r)$ to σ_r . The width ratio $w'_M(\sigma_r)$ is constant regardless of σ_r ; that is,

$$w'_M(\sigma_r) = \frac{w_M(\sigma_r)}{\sigma_r} = w'_{M_c}, \quad (26)$$

where $w'_{M_c} \approx 1.0$ when $\gamma_{23} = 1$ in the formulation of Equation (16). Similarly, we define the height measure $h_R(\sigma_r; \sigma_f)$ of the single-scale filter response as $h_R(\sigma_r; \sigma_f) = R_L(0, 0, z; \sigma_r, \sigma_f)$ and the width measure $w_R(\sigma_r, \sigma_f)$ as the distance $\sqrt{x_0^2 + y_0^2}$ from the z -axis to the circular locus where $R_L(x_0, y_0, z; \sigma_r, \sigma_f)$ gives the half of the maximum response, $h_{M_c}/2$. To compare the widths of the filter response and the original profile, we also introduce the width measure $w_L(\sigma_r)$ of the original line image as the distance $\sqrt{x_0^2 + y_0^2}$ from the z -axis to the circular locus where $L(x_0, y_0, z; \sigma_r)$ gives half of $L(0, 0, z; \sigma_r)$. While σ_r is introduced for the convenience

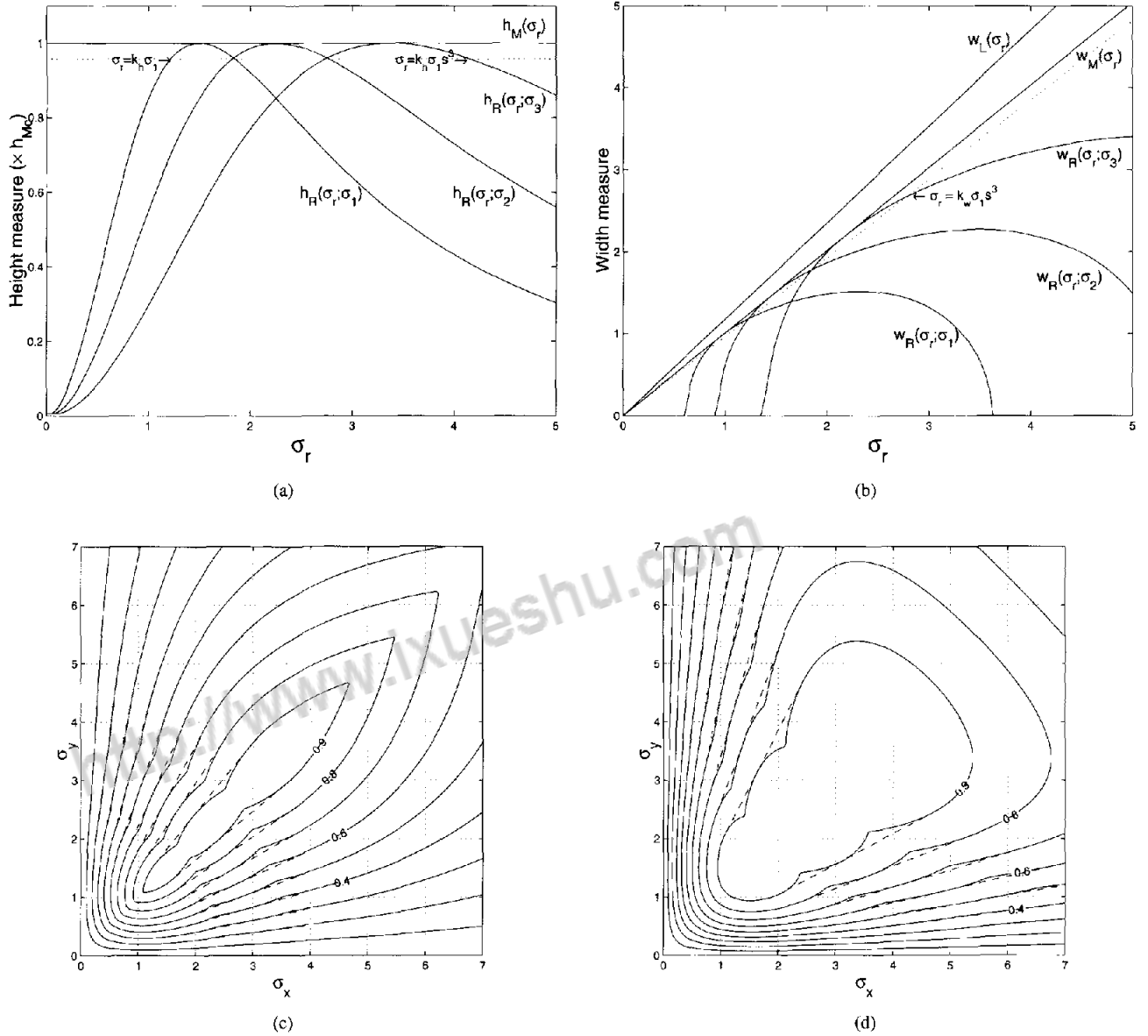


Figure 6. Height and width measures of filter responses in multi-scale integration with $\sigma_i = s^{i-1}\sigma_1$ ($\sigma_1 = 1.5$, $s = 1.5$, $i = 1, 2, 3$). The height measure is normalized so that h_{M_0} is one. (a) Height measures $h_M(\sigma_r) = h_{M_0}$ and $h_R(\sigma_r; \sigma_i)$ for $L(x; \sigma_r)$. (b) Width measures $w_M(\sigma_r) = w_{M_0}$, $w_L(\sigma_r)$ and $w_R(\sigma_r; \sigma_i)$ for $L(x; \sigma_r)$ with $\gamma_{23} = 1$. (c) Height measures for $L_{\text{elliptic}}(x; \sigma_x, \sigma_y)$ with $\gamma_{23} = 1$. Solid lines denote the height measures for the discrete scales. Dashed lines denote the height measures for the continuous scales from σ_1 to σ_3 . (d) Height measures for $L_{\text{elliptic}}(x; \sigma_x, \sigma_y)$ with $\gamma_{23} = 0.5$.

of generating line profiles, $w_L(\sigma_r)$ is for the convenience of comparing the widths of various profile shapes.

Figure 6a and b shows the variations in the height and width measures. Figure 6a gives the plots of $h_R(\sigma_r; \sigma_i)$ at three values of σ_i and $h_M(\sigma_r)$, and Figure 6b shows the plots

of $w_R(\sigma_r; \sigma_i)$ at three values of σ_i , $w_M(\sigma_r)$, and $w_L(\sigma_r)$. The width measure of the multi-scale response is proportional to that of the original line image. In the case of the line image $L(x; \sigma_r)$ with a Gaussian cross-section, $w_L(\sigma_r) \approx 0.9w_M(\sigma_r)$. Although the filter responses make the lines a

Table 1. Height $h_M(\sigma_r)$ and width ratio $w'_M(\sigma_r)$ minima in multi-scale integration at discrete scales using typical scale factors, and σ_r where the minima are taken.

Scale factor s	Min. height $h_{M_{\min}}$	at $\sigma_r = k_h \sigma_i$	Min. width ratio $w'_{M_{\min}}$	at $\sigma_r = k_w \sigma_i$
$s \rightarrow 1$	$h_{M_{\min}} \rightarrow h_{M_c}$	$k_h \rightarrow 1$	$w'_{M_{\min}} \rightarrow w'_{M_c}$	$k_w \rightarrow 0.65$
$s = 1.2$	$h_{M_{\min}} \approx 0.99h_{M_c}$	$k_h \approx 0.92$	$w'_{M_{\min}} \approx 0.99w'_{M_c}$	$k_w \approx 0.59$
$s = \sqrt{2}$	$h_{M_{\min}} \approx 0.97h_{M_c}$	$k_h \approx 0.84$	$w'_{M_{\min}} \approx 0.97w'_{M_c}$	$k_w \approx 0.56$
$s = 1.5$	$h_{M_{\min}} \approx 0.96h_{M_c}$	$k_h \approx 0.82$	$w'_{M_{\min}} \approx 0.96w'_{M_c}$	$k_w \approx 0.55$
$s = 2.0$	$h_{M_{\min}} \approx 0.89h_{M_c}$	$k_h \approx 0.71$	$w'_{M_{\min}} \approx 0.88w'_{M_c}$	$k_w \approx 0.50$

little thinner than the original lines, the multi-scale line filter can be designed so that the width of its responses becomes approximately proportional to the original one.

3.2. Integration of discrete scales

We assumed continuous scales for multi-scale integration in the previous subsection. The response at each scale, however, has to be computed at discrete values of σ_i . In 3-D image filtering, a large amount of computation is necessary to obtain the filter response at each value of σ_i . The maximum and minimum values of σ_i can be determined essentially on the basis of the width range of the anatomical structure of interest. The interval of σ_i should be sufficiently small for the filter response to work uniformly for every line width within the width range, while it is desirable that it should be large enough to minimize the amount of computation required. Thus, we need to determine the minimum number of discrete samples of σ_i which satisfy the following conditions:

- (i) The height measure of the response should be approximately constant within the width range.
- (ii) The width measure of the response should be approximately proportional to the original one within the width range.

Given the discrete samples of σ_i and the assumption of the cross-section shape (here, we use a Gaussian cross section), the accuracy of the approximation can be estimated. Let $\sigma_i = s^{i-1}\sigma_1$ ($i = 1, 2, \dots, n$) be discrete samples of σ_i , where σ_1 is the minimum scale and s is the scale factor determining the sampling interval of σ_i . The multi-scale filter response using the discrete samples of σ_i is given by

$$M(x) = \max_{1 \leq i \leq n} R(x; s^{i-1}\sigma_1). \quad (27)$$

Similarly, the multi-scale filter response using the discrete samples of σ_i for the line image $L(x; \sigma_r)$ is given by

$$M_L(x; \sigma_r) = \max_{1 \leq i \leq n} R_L(x; \sigma_r, s^{i-1}\sigma_1). \quad (28)$$

Given the scale factor s , we can determine $h_{M_{\min}}$ and k_h satisfying

$$h_{M_{\min}} = h_R(k_h \sigma_i; \sigma_i) = h_R(k_h s \sigma_i; \sigma_i), \quad (29)$$

where $\sigma_i = s^{i-1}\sigma_1$ ($i = 1, 2, \dots, n$), $h_{M_{\min}}$ is the minimum of the height measure of the multi-scale response $M_L(x; \sigma_r)$ within the range $k_h \sigma_1 \leq \sigma_r \leq k_h s^n \sigma_1$, and the minimum is taken at $\sigma_r = k_h s^i \sigma_1$ ($i = 0, 1, 2, \dots, n$) (Figure 6a). $h_{M_{\min}}$ can be regarded as a function of the scale factor s . The height measure of the multi-scale response should be sufficiently close to h_{M_c} within the width range of interest. The values of $h_{M_{\min}}$ and k_h at typical scale factors are summarized in Table 1. When $s = 1.5$, $h_{M_{\min}} \approx 0.96h_{M_c}$, which means that the deviation from the continuous case is less than 4%.

With regard to the width measure of the filter response, given the discrete samples of σ_i and the assumption of the profile shape, the accuracy of this approximation can also be estimated. Given the scale factor s , we can determine $w'_{M_{\min}}$ and k_w satisfying

$$w'_{M_{\min}} = \frac{w_R(k_w \sigma_i; \sigma_i)}{k_w \sigma_i} = \frac{w_R(k_w s \sigma_i; \sigma_i)}{k_w s \sigma_i}, \quad (30)$$

where $\sigma_i = s^{i-1}\sigma_1$ ($i = 1, 2, \dots, n$), $w'_{M_{\min}}$ is the minimum of the ratio of $w_M(\sigma_r)$ to σ_r within the range $k_w \sigma_1 \leq \sigma_r \leq k_w s^n \sigma_1$, and the minimum is taken at $\sigma_r = k_w s^i \sigma_1$ ($i = 0, 1, 2, \dots, n$) (Figure 6b). $w'_{M_{\min}}$ can be regarded as a function of the scale factor s . $w'_{M_{\min}}$ should be sufficiently close to w'_{M_c} within the width range of interest. The values of $w'_{M_{\min}}$ and k_w at typical scale factors are summarized in Table 1. When $s = 1.5$, $w'_{M_{\min}} \approx 0.96w'_{M_c}$. When the parameters for the discrete scales of σ_i are $s = 1.5$ and $n = 3$, the ranges of deviation within 4% for the height and the width measures are $0.55\sigma_1 \leq \sigma_r \leq 1.86\sigma_1$ and $0.82\sigma_1 \leq \sigma_r \leq 2.77\sigma_1$ respectively. The range of deviation within 4% for the width measure is shifted to a smaller σ_r than that for the height measure. As a result, the range of deviation of less than 4% for both the height and the width measures is $0.82\sigma_1 \leq \sigma_r \leq 1.86\sigma_1$.

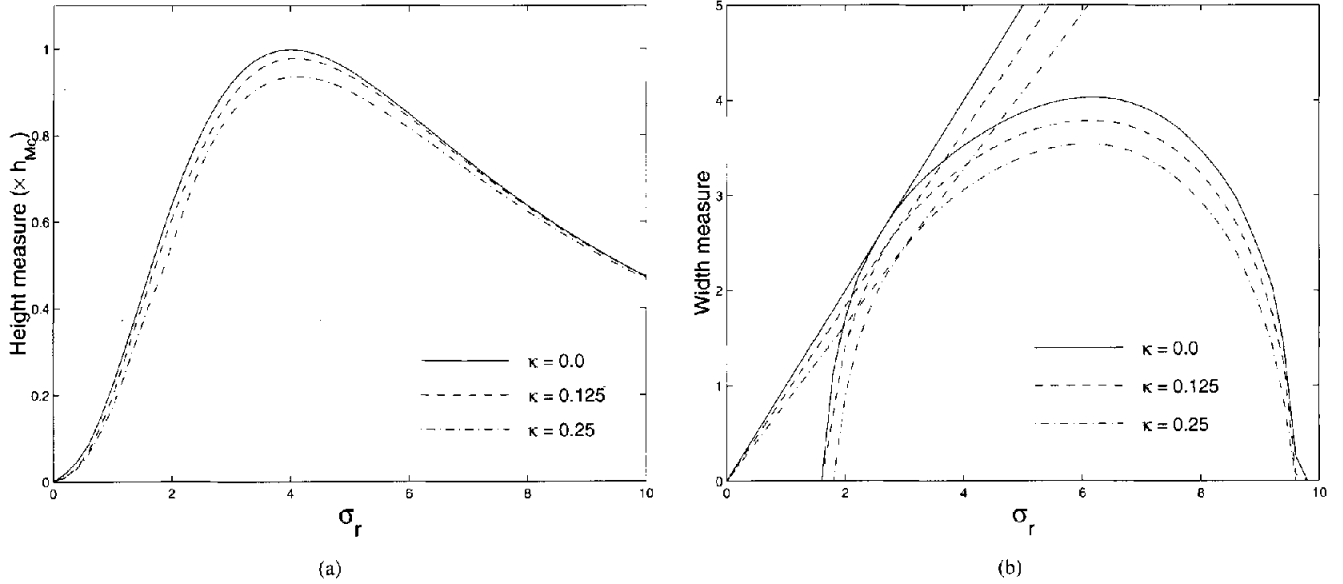


Figure 7. Dependency of height and width measures of filter responses with fixed $\sigma_f (= 4.0)$ for curved line models on σ_r and normalized curvature κ . (a) Height measure for curved line models with $\kappa = 0, 0.125$ and 0.25 . (b) Width measure for curved line models with $\kappa = 0, 0.125$ and 0.25 .

We now extend the experimental analysis of the multi-scale integration to the response to $L_{\text{elliptic}}(\mathbf{x}; \sigma_x, \sigma_y)$ shown in Equation (20). We define the height measure of the filter response of $L_{\text{elliptic}}(\mathbf{x}; \sigma_x, \sigma_y)$ as $h_{R_{\text{elliptic}}}(\sigma_x, \sigma_y; \sigma_f) = R_{L_{\text{elliptic}}}(0, 0, z; \sigma_x, \sigma_y, \sigma_f)$. Figure 6c and d shows the multi-scale integration of the responses at continuous and discrete scales with $\sigma_1 = 1.5$, $s = 1.5$ and $n = 3$ for $\gamma_{23} = 1$ and $\gamma_{23} = 0.5$ respectively. The multi-scale integration using these discrete scales gives a good approximation of that using the continuous scales.

Figure 7 shows the height and width measures of the filter response for curved line models with variable σ_r (see Appendix A.1 for the curved line model). The height and width measures are plotted for three different values of normalized curvature κ when $\sigma_f = 4$ and $\gamma_{23} = \gamma_{12} = 1$. The width was measured along the profile shown in Figure 4a, that is, so that the profile passes through the center of curvature. With κ increasing, the height of the response decreases and the width is underestimated. When $\kappa = 0.25$, the width measure is underestimated about 20% compared with that at $\kappa = 0$, although the reduction of the height measure is less than 10%.

When the line filter is applied to digital images, discretization of input images needs to be considered. Figure 8a shows the height measure plots when the input line image and its response are given as discrete samples $L(i, j, k; \sigma_r)$ and $R_L(i, j, k; \sigma_r, \sigma_f)$ ($i, j, k = \dots, -2, -1, 0, 1, 2, \dots$).

Figure 8b shows the height measure plots in the case of continuous images. In the filtering of discrete images, the aliasing effect cannot be ignored when σ_r or σ_f is small, especially when either is less than 1 pixel. Because the visualization of small structures is often of primary interest, the behavior at small scales requires particular attention. As shown in Figure 8a, the filter response behaves sufficiently well in the range $\sigma_f \geq 1.0$ pixel and $\sigma_r \geq 1.0$ pixel. Although the filter responses are affected by the aliasing effect in the range $\sigma_f < 1.0$ pixel, the difference between h_{Mc} and the filter responses is still less than 7% in the range $\sigma_f \geq 0.8$ pixel. Furthermore, the filter response at $\sigma_f = 0.8$ pixel approximates h_{Mc} for the discrete unit impulse [in the case of $\sigma_r \rightarrow 0$ in $L(i, j, k; \sigma_r)$], which is given by

$$L_\delta(i, j, k) = \begin{cases} 1, & i = j = 0 \\ 0, & \text{otherwise.} \end{cases} \quad (31)$$

Considering the above advantageous characteristics, we utilize $\sigma_f = 0.8$ pixel as the minimum scale up to which the responses to the discrete images can be regarded as giving a reasonable approximation of the continuous images.

In the above, we have assumed that the cross-section of the line has a Gaussian shape. A similar analysis can, however, be made for other cross-sectional shapes. In the case of a line with a pill-box shape, for example, in which cross sections are

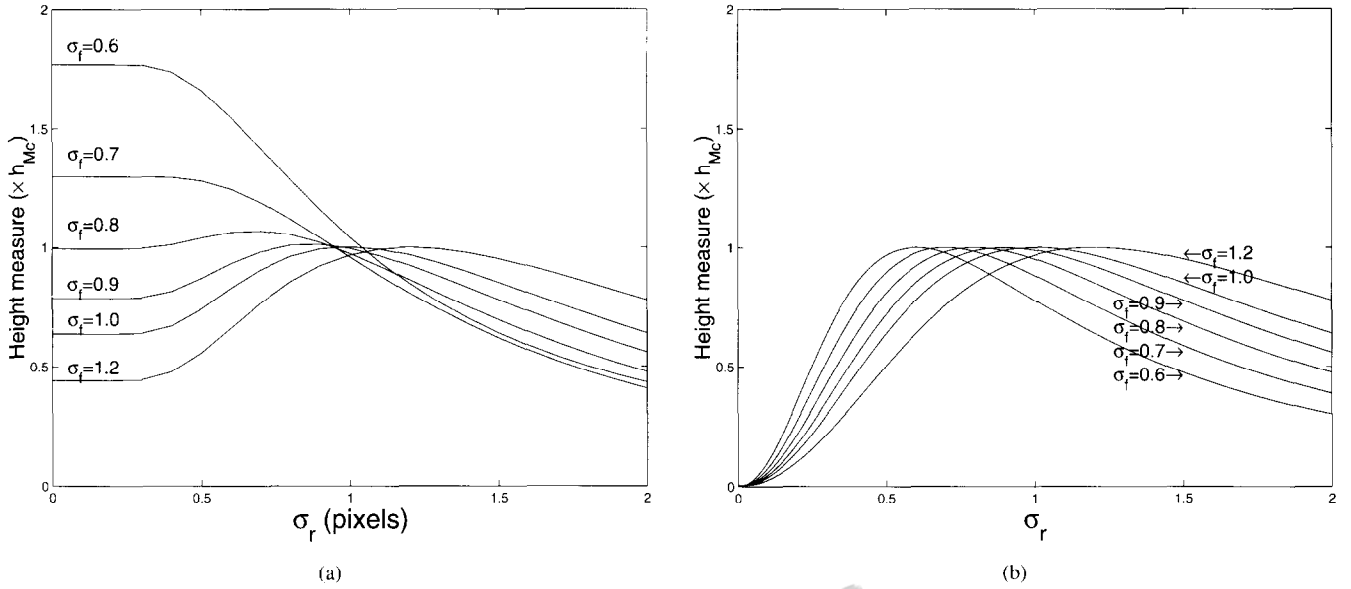


Figure 8. Height measures with small σ_f for discrete and continuous images. (a) Height measures $h_R(\sigma_r; \sigma_f)$ with small σ_f for discrete images ($\sigma_f = 0.6, 0.7, 0.8, 0.9, 1.0$ and 1.2 pixel). (b) Height measures $h_R(\sigma_r; \sigma_f)$ with small σ_f for continuous images ($\sigma_f = 0.6, 0.7, 0.8, 0.9, 1.0$ and 1.2).

given by

$$L_p(\mathbf{x}; \sigma_r) = \begin{cases} 1, & \sqrt{x^2 + y^2} \leq \sigma_r \\ 0, & \text{otherwise,} \end{cases} \quad (32)$$

where $h_{M_{\min}} \approx 0.93h_{Mc}$ and $w'_{M_{\min}} \approx 0.95w'_{Mc}$ for $s = 1.5$. The relation between the width measures of the original line images and the multi-scale line-filtered responses is given by $w_L(\sigma_r) \approx 0.82w_M(\sigma_r)$. In this case, the filter responses make lines thinner than the Gaussian cross sections.

In summary, we have formulated and analyzed a multi-scale 3-D line filter with discrete scales. Combining Equations (22) and (27), we have,

$$M(\mathbf{x}) = \max_{1 \leq i \leq n} \{\sigma_i^2 \cdot \lambda_{123}(\mathbf{x}; \sigma_i)\}, \quad (33)$$

where $\sigma_i = s^{i-1}\sigma_1$. When $s = 1.5$ and a Gaussian cross-section shape is assumed, Equation (33) can be regarded as providing a reasonable approximation of the multi-scale integration of the continuous case in the sense that the deviation from the continuous case is less than 4% with respect to both the height and width measures.

4. PRACTICAL ASPECTS OF THE METHOD

4.1. Sinc interpolation for obtaining isotropic voxels

Because 3-D medical images typically have high in-plane resolution but relatively low axial resolution, careful consideration of the non-isotropic resolution is needed for the convolution with Gaussian derivatives. To apply isotropic Gaussian filters, it is necessary to use a different value (in pixels) of the standard deviation of Gaussian for the axial direction if the aspect ratio of the in-plane and axial dimensions of the voxel deviates from one. When the standard deviation of Gaussian is small, however, the sampling interval along the axial direction often becomes too large to approximately satisfy the Nyquist criteria. Our approach is to apply interpolation along the axial direction using a sinc function before line filtering to obtain isotropic voxels. There are various alternative interpolation methods such as the tri-linear and B-spline methods, but only sinc interpolation guarantees the recovery of the original information, thereby allowing the performance of the 3-D line filter itself to be determined. Sinc interpolation is performed by zero-filled expansion in the frequency domain. Maximum-intensity projection (MIP) results have been reported to be significantly improved even by using sinc interpolation along the axial direction (Hylton *et al.*, 1992; Du *et al.*, 1994). This procedure can be used to

improve the in-plane resolution as well. We therefore employ sinc interpolation both for improved visualization and the proper computation of Gaussian derivatives.

4.2. Selection of parameter values

The multi-scale line filter includes several parameters. In defining the generalized line measure γ_{23} , γ_{12} and α in Equation (16) need to be specified, while in the multi-scale integration, the smallest scale σ_1 , the scale factor s , and the number of scale levels n in Equation (33) need to be specified.

With regard to the parameters in the line measure, if there are strong sheet structures to be removed from an image, γ_{23} should be 1.0. If the cross-sections of line structures of interest vary not only in size but also in shape, γ_{23} should be 0.5. γ_{12} should also be determined to optimize the trade-off between the preservation of branches and the reduction of noise and spurious branches. However, the performance has been found to be relatively insensitive to the values of γ_{23} and γ_{12} as long as they are between 0.5 and 1.0. When $\gamma_{23} = \gamma_{12} = 1.0$, $\alpha = 0.25$ can be considered a good compromise as shown in Figure 5e.

With respect to the parameters in multi-scale integration, we showed in Section 3 that s should be 1.5 or less for a reasonable approximation of the multi-scale integration using the continuous scales. Suitable values for σ_1 and n should be found for each case, taking into account the anatomical structure of interest, the imaging modality and imaging parameters such as the field of view (FOV). However, we confirmed that the results were quite stable for different images obtained under similar conditions once suitable values have been determined.

4.3. Computation of second derivatives of Gaussian and eigenvalues

The computation of the second derivatives of Gaussian in the Hessian matrix was implemented using three separate convolutions with 1-D kernels as represented by

$$\begin{aligned} I_{x^i y^j z^k}(\mathbf{x}; \sigma_f) &= \left\{ \frac{\partial^2}{\partial x^i \partial y^j \partial z^k} G(\mathbf{x}; \sigma_f) \right\} * I(\mathbf{x}) \\ &= \frac{d^i}{dx^i} G(x; \sigma_f) * \left\{ \frac{d^j}{dy^j} G(y; \sigma_f) * \left\{ \frac{d^k}{dz^k} G(z; \sigma_f) * I(\mathbf{x}) \right\} \right\} \end{aligned} \quad (34)$$

where i , j , and k are non-negative integers satisfying $i + j + k = 2$, and $3\sigma_f$ was used as the radius of the kernel. Using this decomposition, the amount of computation needed can be reduced from $O(n^3)$ to $O(3n)$, where n is the kernel diameter.

The eigenvalues were computed using Jacobi's method. A numerical problem could exceptionally occur in this computation for synthesized images of the mathematical line models

without noise. However, the numerical problem could be avoided by adding a very small amount of Gaussian noise. We did not have such a numerical problem in the experiments using MR and CT images since noise is essentially involved in real images.

4.4. Implementation on a multi-CPU machine

The method was implemented on a Sparc Enterprise Server (Sun Microsystems, Mountain View, CA) with eight CPUs (Ultra Sparc, 168 MHz; Sun Microsystems) and 1 Gbyte main memory using multi-threaded programming (Lewis and Berg, 1996). In Section 3, we showed a method of minimizing the number of scales for line filtering to be computed, while maintaining an approximately equalized response at each scale within the width range. Nevertheless, 3-D image filtering for several scales still requires a large amount of computation. The method, including sinc interpolation by DFT and the subsequent multi-scale line filtering by convolution and eigenvalue computation, can, however, be easily parallelized and naturally implemented on a multi-CPU machine using multi-threaded programming. We confirmed that the computational speed was almost proportional to the number of CPUs. Using eight CPUs, about 5 and 10 min were required to compute sinc interpolation from $256 \times 256 \times 30$ pixels to $256 \times 256 \times 102$ pixels, and multi-scale line filtering with three scales ($\sigma_1 = 1.5$ pixels, $s = 1.5$ and $n = 3$) respectively.

5. EXPERIMENTAL RESULTS

We evaluated the method using MRA images of brain vessels, MR images of the brain and CT images of the lung and abdomen, aiming at the segmentation and visualization of brain vessels from the MRA and MRI, bronchi from a chest CT and liver vessels (portal veins) from an abdominal CT.

5.1. Brain vessel segmentation from MRA

In this experiment, we used phase-contrast MRA images (Dumoulin *et al.*, 1989) of the brain. The MRA data of the cerebral veins are obtained routinely for surgical planning and navigation of brain tumor resection at the Surgical Planning Laboratory, Brigham and Women's Hospital. The position of the tumor can be localized by using the 3-D vein structures as landmarks or road maps before and during surgery (Kikinis *et al.*, 1996; Nakajima *et al.*, 1997). The improvement of small-vessel visibility and continuity facilitates the reliable and efficient use of the 3-D vein model for interactive planning and intra-operative navigation. This is one of our main motivations for the development of line filtering.

The MRA data consisted of two sets of 60 sagittal slices of 256×256 pixels. One set comprised the velocity magnitude images and the other the simultaneously detected stationary

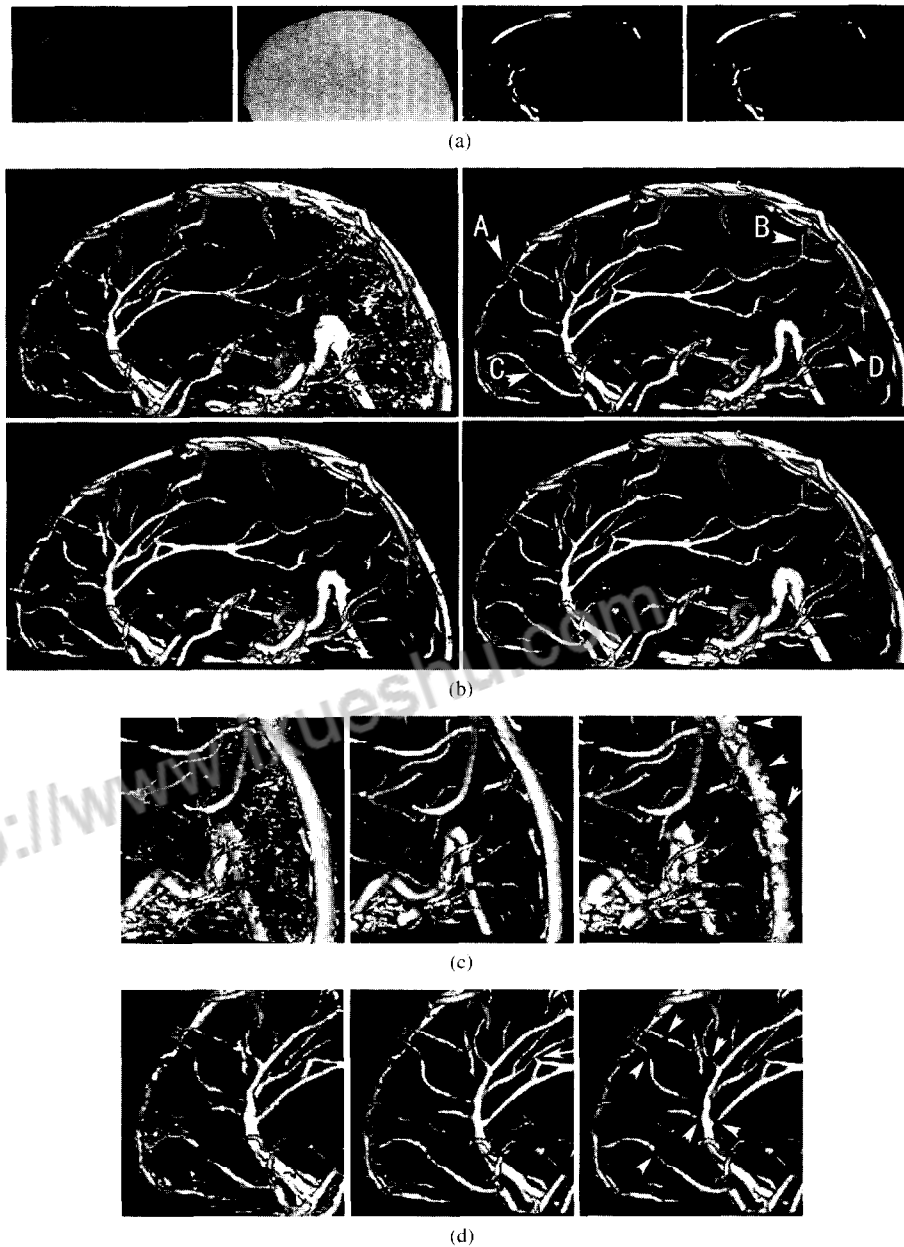


Figure 9. Brain vessel segmentation from MRA. (a) Input slice images. From left to right: stationary tissue image, binary stationary tissue image used as a mask, velocity image and masked velocity image. (b) Surface rendering of segmented vessels with different shapes of $w_{23}(\lambda_2; \lambda_3)$. Upper left, original images; upper right, line-filtered images with $\gamma_{23} = \gamma_{12} = 1.0$, and $\alpha = 0.25$ (letters represent the correspondence relations with Figure 10); lower left, line-filtered images with $\gamma_{23} = \gamma_{12} = 0.5$ and $\alpha = 0.25$; lower right, combined result of line-filtered images with $\gamma_{23} = \gamma_{12} = 1.0$ and $\alpha = 0.25$ and original images with relatively high threshold. (c) and (d) Surface rendering of segmented vessels with different shapes of $w_{12}(\lambda_1; \lambda_2)$. (c) Left, original images; middle, line-filtered images with $\gamma_{23} = \gamma_{12} = 1.0$ and $\alpha = 0.25$ —the noise is significantly reduced; right, line-filtered images with $\gamma_{23} = \gamma_{12} = 1.0$ and $\alpha \rightarrow 0$; the vessel surfaces are jagged (indicated by arrowheads). (d) Left, original images; middle, line-filtered images with $\gamma_{23} = \gamma_{12} = 1.0$ and $\alpha = 0.25$ —the overall vessel continuity is improved, although there is evidence of an unwanted connection (indicated by arrow), in our experience such unwanted connections are rare; right, line-filtered images with $\gamma_{23} = \gamma_{12} = 1.0$ and $\alpha = 1.0$ —the vessels are susceptible to fragmentation (indicated by arrowheads).

tissue images. The pixel dimensions were $0.78 \times 0.78 \text{ mm}^2$, while the slice thickness was 0.8 mm. The images were taken from a patient with arterio-venous malformation (AVM). Although this image set was not obtained for surgical navigation purposes, we used this set because both MRA and DSA images obtained from the same patient were available. DSA images are currently regarded as the gold standard of vessel imaging, and are superior in both resolution and contrast to MRA, especially with regard to the visibility of small vessels. The results of line filtering can thus be well evaluated by comparing them with the DSA images.

We trimmed a region of 240×115 pixels from each slice. Since the voxel was almost isotropic in this case, we did not perform sinc interpolation between slices. We applied line filtering to the velocity magnitude images using $\sigma_1 = 0.8$ pixel, $s = 1.5$ and $n = 3$ as the parameter values for multi-scale integration. The stationary tissue images were thresholded to obtain binary images and the largest connected 3-D component was extracted. The resultant binary images including only the largest component almost corresponded to the brain tissue region and were used as a mask for the line-filtered images. We multiplied the mask images by the line-filtered images, thresholded the masked line-filtered images using an appropriate threshold value and removed small components whose size was less than 10 voxels. The original velocity magnitude images were processed in the same manner for comparison purposes. Finally, the line-filtered binary images and the original images were rendered by a surface rendering technique (Schroeder *et al.*, 1996). Figure 9a shows the stationary tissue image, and binary stationary tissue image used as a mask, velocity magnitude image, and masked velocity magnitude image.

We applied line filtering using several sets of parameter values. The aim of the experiment was to enable a comparison to be made among line-filtered images using different shapes of $w_{12}(\lambda_1; \lambda_2)$ [Equation (15)] and $w_{23}(\lambda_2; \lambda_3)$ [Equation (13)], as well as between the line-filtered and original images. Figure 9b shows the rendered results for the original and the line-filtered images using $\gamma_{23} = \gamma_{12} = 1.0$ and $\gamma_{23} = \gamma_{12} = 0.5$ with the same $\alpha (= 0.25)$. The combined images of the original and line-filtered images are also shown, which are the union of the line-filtered images ($\gamma_{23} = \gamma_{12} = 1.0$) and original images thresholded using a relatively high value. Figure 10 is the DSA image at an artery phase of the same patient. Comparison with the DSA image confirms the line-filtered images are superior to the original ones with respect to the visibility of small vessels, vessel continuity, and the reduction of noise and artefacts. However, the large vessel in the lower right-hand corner was considerably thinned in the line-filtered images. The combined images gave a good visualization for both small and large vessels. The difference

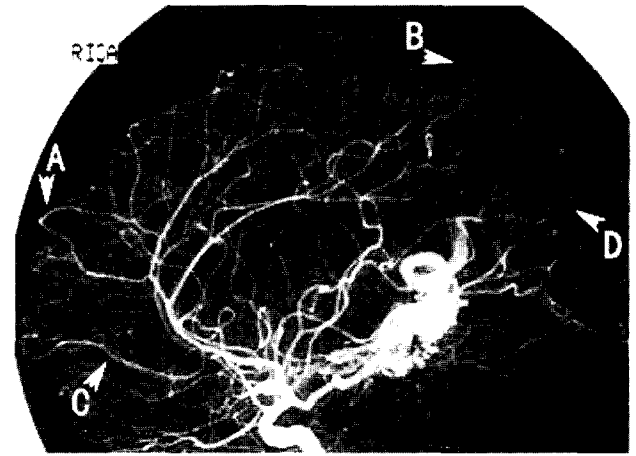


Figure 10. DSA image at an artery phase of the same patient whose MRA images are used in Figure 9. The letters represent correspondence relations with the upper right-hand frame of Figure 9b.

between the results for $\gamma_{23} = \gamma_{12} = 1.0$ and $\gamma_{23} = \gamma_{12} = 0.5$ was subtle; when $\gamma_{23} = \gamma_{12} = 1.0$, the continuity of thin vessels was slightly better. Although we also applied conventional Gaussian smoothing to the original images, small vessels were corrupted more than the noise was reduced, giving results that are inferior to the original images.

Figure 9c and d shows the rendered results using different α values in $w_{12}(\lambda_1; \lambda_2)$ with the same γ_{23} and $\gamma_{12} (= 1.0)$. The same threshold value was used for the line-filtered images in both these cases. In the result using $\alpha \rightarrow 0$ (Figure 9c, right-hand frame), the surfaces of the vessels are seen to be jagged, and spurious bump structures were extracted, which are similar to the upper frame of Figure 4b. In the result with $\alpha = 1.0$ (Figure 9d, right-hand frame), the vessels were easily fragmented. Overall, the result with $\alpha = 0.25$ was superior in terms of both vessel continuity and the smoothness of the vessel surfaces. These results are consistent with the simulation experiments shown in Figures 4 and 5.

5.2. Bronchus segmentation from chest CT

In this experiment, we used chest CT images taken by a helical CT scanner. The aim was to construct the 3-D map of bronchus structures for path planning in biopsy using bronchoscopy. The CT data comprised 30 slices of 512×512 pixels; the pixel dimensions were $0.29 \times 0.29 \text{ mm}^2$. The beam width was 1 mm and the reconstruction pitch was 1 mm.

We trimmed a region of 256×256 pixels from each slice. The airway regions of the bronchi in the trimmed images were carefully hand-segmented by one of the authors (NS), a radiology specialist, and used as the gold standard. In order to adjust the range of the CT values to the range corresponding to the airways of the bronchi, the intensity level $I(\mathbf{x})$ was

converted to $I'(x)$ using

$$I'(x) = \begin{cases} 0, & I(x) \geq I_{\max} \\ -(I(x) - I_{\max}), & I(x) < I_{\max}. \end{cases} \quad (35)$$

Since the airway regions are darker than surrounding regions, the brightness was also inverted in Equation (35). We used $I_{\max} = -820$ in this experiment. The line filtering was most effective for the images converted using $I_{\max} = -820 \pm 40$. (We tested another two sets of chest CT data, and the intensity level conversion using Equation (35) with $I_{\max} = -820$ was also highly effective in these cases.) Sinc interpolation was performed for the trimmed and intensity-converted images and 102 slices were reconstructed. Line filtering was applied to the interpolated images using $\gamma_{23} = \gamma_{12} = 0.5$, $\alpha = 0.25$, $\sigma_1 = 1.5$ pixels, $s = 1.5$ and $n = 3$ as the parameter values for the line filtering. In this case, the line structures of interest were relatively thick in terms of pixels. Thick structures tend to possess variations in cross-sectional shape, that is, the cross section deviates from a circular shape. In addition, quite a few junctions of branches were easily fragmented in this case. Thus, better results were obtained when $\gamma_{23} = \gamma_{12} = 0.5$. We also applied conventional Gaussian filtering ($\sigma = 0.8$) to the interpolated images for comparison purpose. These filtered images and the original images were thresholded. The manually segmented images were also interpolated so as to give 102 slices. The binary images obtained were rendered by the surface rendering technique.

Figure 11a shows the original CT image and its converted image using Equation (35). Figure 11b shows manually segmented images. Figure 11c shows the rendered results of the original, Gaussian-filtered and line-filtered images. The line-filtered images post-processed by removing connective regions with less than 400 voxels is also shown. This is a typical post-processing procedure after thresholding to remove noise components. The line-filtered images (Figure 11c, lower left-hand frame), significantly improved the recovery of the small branches and the continuity of the bronchi. The stenotic part of a bronchus is also clearly observable in the line-filtered images. Although the Gaussian filtered images (Figure 11c, upper right-hand frame) also reduced noise, the improvement was much smaller than in the case of the line-filtered images. There are many other air regions in the lung, which should have similar CT values to the bronchial airways. The line filter could effectively discriminate the bronchial airways using the local shape information. By applying the post-processing of small-region removal, noise was removed and the depiction of the bronchi was considerably improved especially in peripheral structures (Figure 11c, lower right-hand frame).

Figure 11d shows the intersection of original and line-filtered images shown in the upper and lower left-hand frames

of Figure 11c (left-hand frame), the difference of the intersection and original images (middle frame) and the difference of the intersection and line-filtered images (right-hand frame). Figure 11d means that the line filtering removed the components shown in the middle frame (where noise components are dominant) from the original images to obtain the components in the left frame and further added the components in the right frame (where airway components are dominant). Figure 11e shows the line-filtered result at each scale, intuitively demonstrating the usefulness of a combination of multi-scale responses.

Figure 11f–h depicts some illustrative examples showing the effects of line filtering. Figure 11f shows close-ups of the branches in the upper left-hand corner of the line-filtered images using $\gamma_{12} = 1$ (left) and $\gamma_{12} = 0.5$ (right), demonstrating that the branches were easier to be fragmented when $\gamma_{12} = 1$. Figure 11g shows close-ups of the peripheral parts of bronchi in the post-processed line-filtered (left) and manually segmented (right) images. The depiction of branching at peripheral parts was clearer in the line-filtered images. Figure 11h shows close-ups of the stenotic part of a bronchus in the post-processed line-filtered (upper) and manually segmented (lower) images. In Figure 11g and h, the difference in width was large between the line-filtered and manually segmented images. This difference originated from the threshold level to define the airway regions. The airway regions were extracted so as to include the lower slopes of the profiles in manual segmentation, while the threshold value had to be high enough in the line-filtered images not to include noise components as much as possible. In spite of the difference in absolute width, the width in one image was well correlated to that in the other.

To make a quantitative comparison between the original and several kinds of filtered images, we calculated the fractions of true positive detections and false positive detections at various threshold values, and plotted them as curves, which are similar to receiver operating characteristic (ROC) curves (Goodenough *et al.*, 1974). We used the manually segmented images and its 3-D thinned images as the gold standard. In the manually segmented images, the voxel value was one if it was in an airway region, and zero otherwise. We regarded a voxel with a value of one in the 3-D thinned images as an airway center line point. The fraction of true positive detections T_p was defined by

$$T_p = \frac{N_{td}}{N_t} \quad (36)$$

where N_{td} is the number of the detected airway center line points and N_t is the total number of the airway center line points. The fraction of false positive detections F_p was defined by

$$F_p = \frac{N_{fd}}{N_d} \quad (37)$$

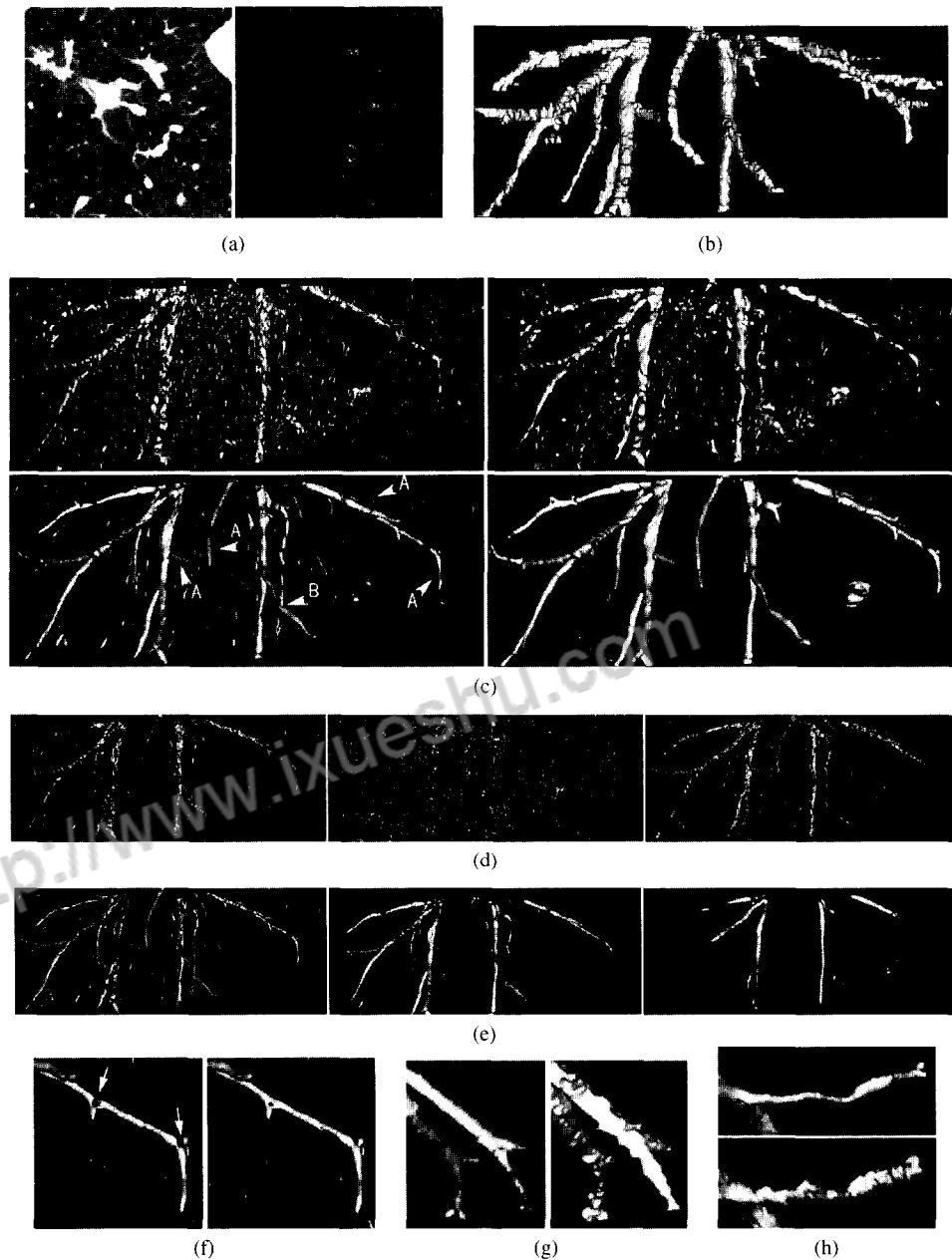


Figure 11. Bronchus segmentation from lung CT images. (a) Input images. Left, original image; right, intensity-converted image. (b) Surface rendering of manually segmented bronchial airways. (c) Surface rendering of segmentation results. Upper left, original image; upper right, Gaussian-filtered image; lower left, line-filtered image—the visibility was greatly improved, not only of the small branches (indicated by A) but also of the stenotic part (indicated by B); lower right, line-filtered image post-processed by removing connective regions with less than 400 voxels—the depiction of peripheral structures was considerably improved. (The blob structure in the lower right-hand corner is an air region surrounding by a tumor.) (d) Intersection and differences of original and line-filtered images. Left, intersection of original and line-filtered images; middle, difference of the intersection and line-filtered images. (e) Surface rendering of segmented bronchi of single-scale line-filtered images. Left, $\sigma_f = 1.5$; middle, $\sigma_f = 1.5 \times 1.5$; right, $\sigma_f = 1.5 \times 1.5^2$. (f) Branches in line-filtered images. Left, $\gamma_{12} = 1$. Branches were easier to be fragmented (indicated by arrows). Right, $\gamma_{23} = 0.5$. (g) Peripheral bronchi. Left, post-processed line-filtered image; right, manually segmented image. (h) Stenotic segment. Left, post-processed line-filtered image; right, manually segmented image.

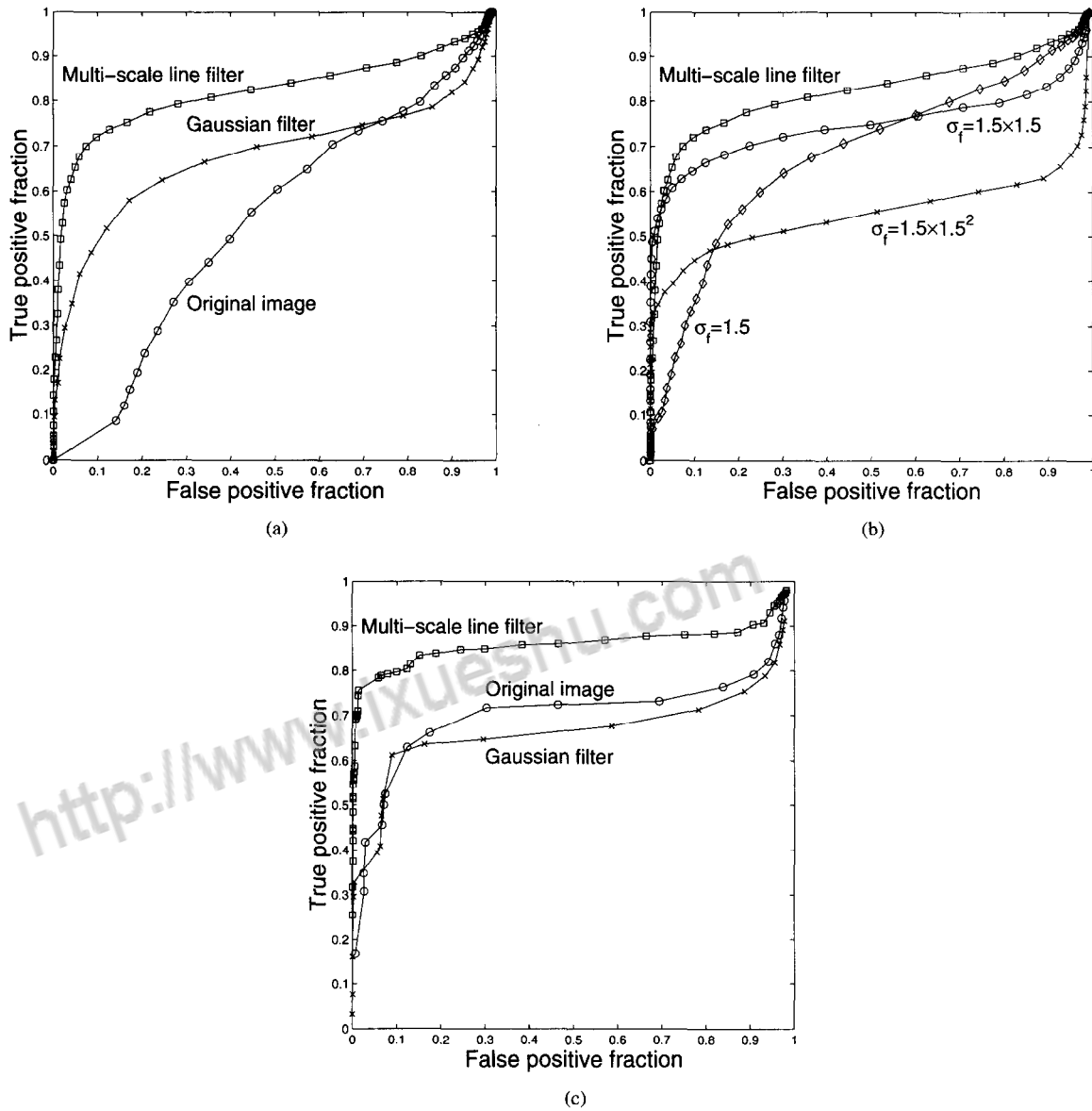


Figure 12. Results of ROC-like analyses for bronchus segmentation from lung CT images. (a) Comparison of original, Gaussian-filtered and line-filtered images. (b) Comparison of single-scale and multi-scale line-filtered images. (c) Comparison of original, Gaussian-filtered and line-filtered images after removing connective regions with less than 400 voxels.

where N_{fd} is the number of the detected points not included in the airway regions and N_d is the total number of the detected points. When $T_p = 1$ and $F_p = 0$, the detection is considered to be ideal in the sense that all the airway center line points can be detected and no points are detected outside the airway regions.

Figure 12 shows the results of the quantitative evaluation by the ROC-like analysis described above. T_p and F_p are

plotted with a gradually changing threshold value. At the upper left-hand corner, $T_p = 1$ and $F_p = 0$. When the curves are closer to the upper left-hand corner, the detection is considered to be more successful. In Figure 12a, the multi-scale line-filtered images are compared with the original and Gaussian-filtered images, and is shown to be highly effective for bronchus extraction. Figure 12b illustrates the improved result obtained with multi-scale integration as compared with

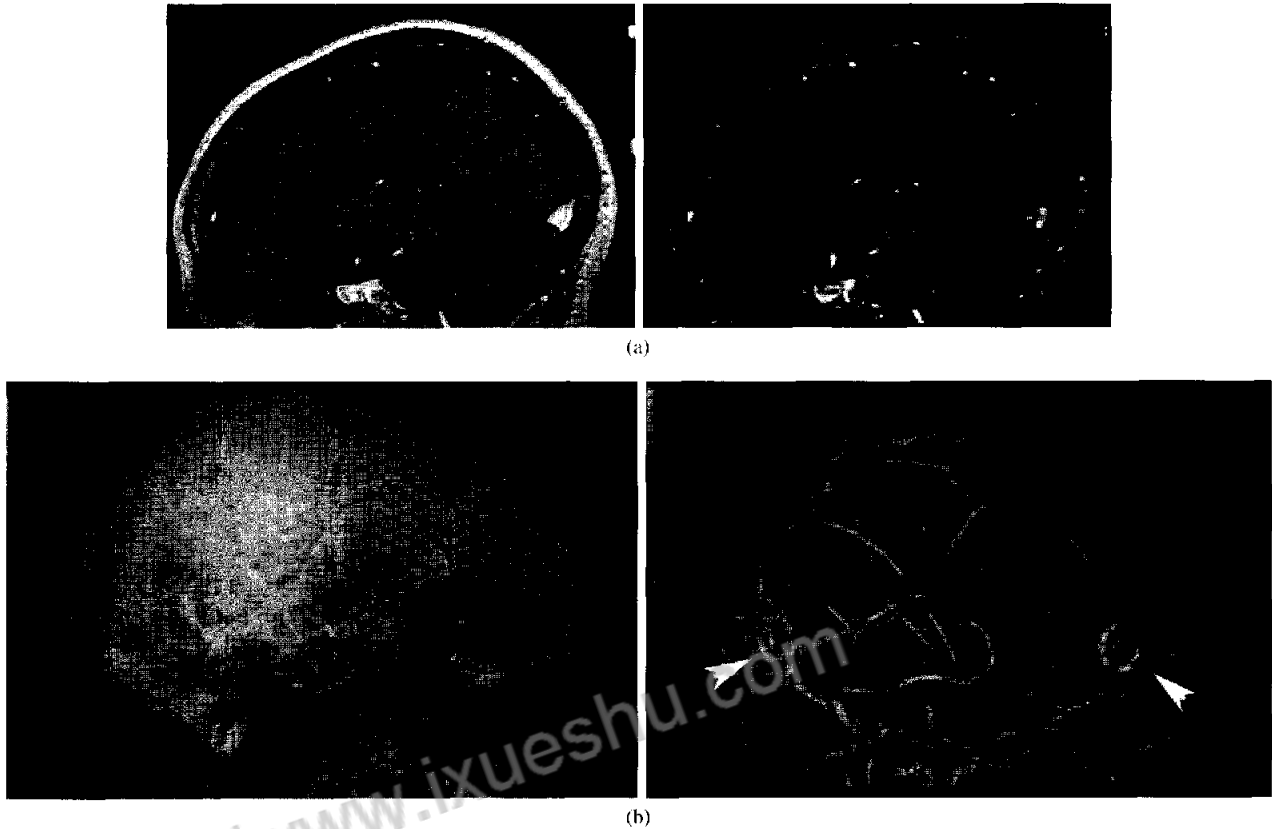


Figure 13. Brain vessel visualization from MR (magnetic resonance) images. Movies in the video. (a) Input original (left) and line-filtered image (right). (b) Volume-rendered images. Left, original images; right, line-filtered images. The line filter gave a high level of response to the rims of the biopsy holes (indicated by arrowheads) as well as to vessel structures.

that obtained at each single scale, indicating that multi-scale integration is quite effective. Figure 12c shows the comparison of the post-processed results in which connective regions with less than 400 voxels were removed. It can be seen that after the post-processing as well, the multi-scale line-filtered images are significantly better than the original and Gaussian-filtered images for constructing the 3-D map of bronchial tree structures.

5.3. Brain vessel visualization from MRI

In this experiment, we used post-contrast gradient-echo (SPGR) MR images of the brain. The aim was to visualize the vein structures used as landmarks for brain tumor resection with the minimum amount of interactive segmentation burden. Since MR images contains various structures other than vessels unlike MRA data, the segmentation of vessels often involves complex manual operations. The MRI data set consisted of 192 sagittal slices of 256×256 pixels. The pixel dimensions were $1.0 \times 1.0 \text{ mm}^2$, while the slice thickness was 1.2 mm. The DSA images obtained from the same patient

were also available, and used to compare with the vessel visualization with the MRI data.

We used 80 slices corresponding to the right half of the head, and trimmed a region of 220×150 pixels from each slice. Sinc interpolation was performed for the trimmed images and 96 slices were reconstructed. Line filtering was applied to the interpolated images using $\gamma_{23} = \gamma_{12} = 1.0$, $\alpha = 0.25$, $\sigma_1 = 0.8$ pixel, $s = 1.5$ and $n = 3$. The original and line-filtered images were visualized using the volume rendering technique (Levoy, 1988; Lacroute and Levoy, 1994).

Figure 13a shows the original and line-filtered MR images. Figure 13b shows the volume-rendered images of the original and line-filtered images. Figure 14 shows the DSA image at a vein phase of the same patient. It is quite difficult to perceive the vessels through the skin in the volume-rendered original images, but almost the same vein structures as in the DSA image can be clearly seen in the volume-rendered line-filtered images. Although the vessels and the skin had almost the same intensity level in the original images, the line filter could mostly remove the effect of the skin since it has a sheet-like

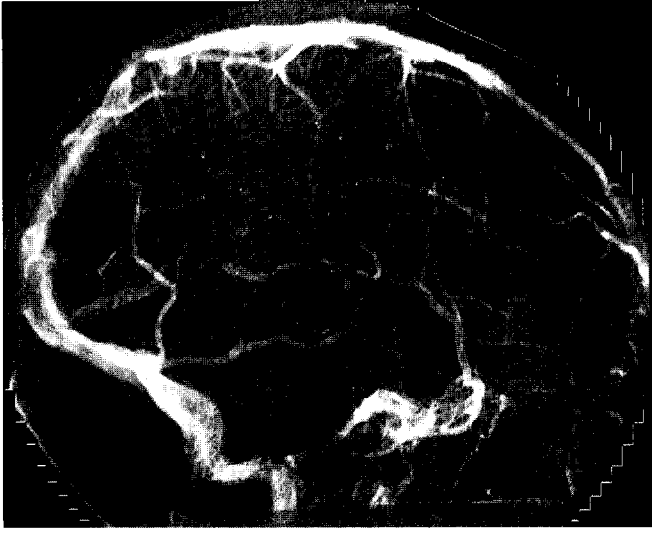


Figure 14. DSA image at a vein phase of the same patient whose MR images are used in Figure 13.

structure. This experiment demonstrated the usefulness of the ability to discriminate between line and sheet structures.

The patient from whom these images were obtained had a brain tumor and there were biopsy holes in the skin and skull; the line filter also gave high levels of response to the rims of these biopsy holes. It is a current limitation of our formulation that the line filter gives a high level of response to rim structures as well as to line structures. In order to remove rim structures, a procedure such as the non-linear combination of the first derivatives for line detection from 2-D images (Vandarbrug, 1975; Koller *et al.*, 1995) needs to be extended for use with 3-D images.

5.4. Liver vessel segmentation from abdominal CT

In the final experiment, we used abdominal CT images taken by a helical CT scanner. The aim was to segment the portal veins to localize a tumor with the relation to them for surgical planning. The CT data set consisted of 43 slices of 512×512 pixels; the pixel dimensions were $0.59 \times 0.59 \text{ mm}^2$. The beam width was 3 mm and the reconstruction pitch was 2.5 mm. The CT data were imaged using CTAP (CT arterial portography)^a; the portal veins had high CT values due to the injection of contrast material.

We trimmed a region of 400×400 pixels from each slice, which included the whole liver. The liver regions in the trimmed images were roughly hand-segmented by a radiology

specialist and used as a mask. In order to adjust the range of the CT values to the range corresponding to the intensity variation inside the liver, the intensity level $I(\mathbf{x})$ was converted to $I'(\mathbf{x})$ using

$$I'(\mathbf{x}) = \begin{cases} 0, & I(\mathbf{x}) \leq I_{\min} \\ I(\mathbf{x}) - I_{\min}, & I_{\min} < I(\mathbf{x}) < I_{\max} \\ I_{\max} - I_{\min}, & I(\mathbf{x}) \geq I_{\max} \end{cases} \quad (38)$$

We used $I_{\min} = 1000$ and 1300 in this experiment. More than five sets of CTAP data were tested, and line filtering was also found to be effective using this conversion. The sizes of the trimmed and intensity-converted images were reduced to half using the Laplacian pyramid (Burt and Adelson, 1983) to reduce a computational amount to a practical level. Since interpolation was performed and 91 slices of 200×200 pixels were reconstructed. The hand-segmented images of the liver regions were also reduced and interpolated so as to give 91 slices of 200×200 pixels. Line filtering was applied to the interpolated images using $\gamma_{23} = \gamma_{12} = 1.0$, $\alpha = 0.25$, $\sigma_1 = 0.8$ pixels, $s = 1.5$ and $n = 2$. We multiplied the mask images with the line-filtered images, thresholded the masked line-filtered images using an appropriate threshold value, and removed small components whose size was less than 10 voxels. The binary versions of the images before line filtering were also obtained in the same manner for comparison purposes. Finally, the obtained binary images were rendered by the surface rendering technique.

Figure 15a shows the intensity-converted image of the original CT data and its masked version. Figure 15b shows the rendered results. In Figure 15b, the left-hand frame gives the rendered result of the original binary images, and the right-hand frame shows a combination of the line-filtered binary images for small-vessel detection and the original binary images using relatively high threshold values for large-vessel detection. The two binary images were combined by taking the union of them. The CT data were scanned when the contrast material in the portal vein began to be absorbed by the liver tissues, as seen in the lower part of Figure 15b. Such a condition is quite common in CTAP for portal vein imaging. In the original images, the small vessels appear buried due to the contrast material absorbed by the liver tissue. However, in the combined result of the original and line-filtered images, not only is the nonuniformity of the contrast material canceled out, but also the recovery of small vessels is significantly improved over the entire liver area. The line filter inherently cuts low-frequency components since it is based on second derivatives. Thus, the nonuniformity of contrast material which has relatively low-frequency components was effectively reduced.

^aThe CT data were obtained by a helical CT scanner with the 20 s delay following the administration of contrast material using a catheter inserted in the superior mesenteric artery (SMA). This method of portal vein imaging is called CT arterial portography (CTAP).

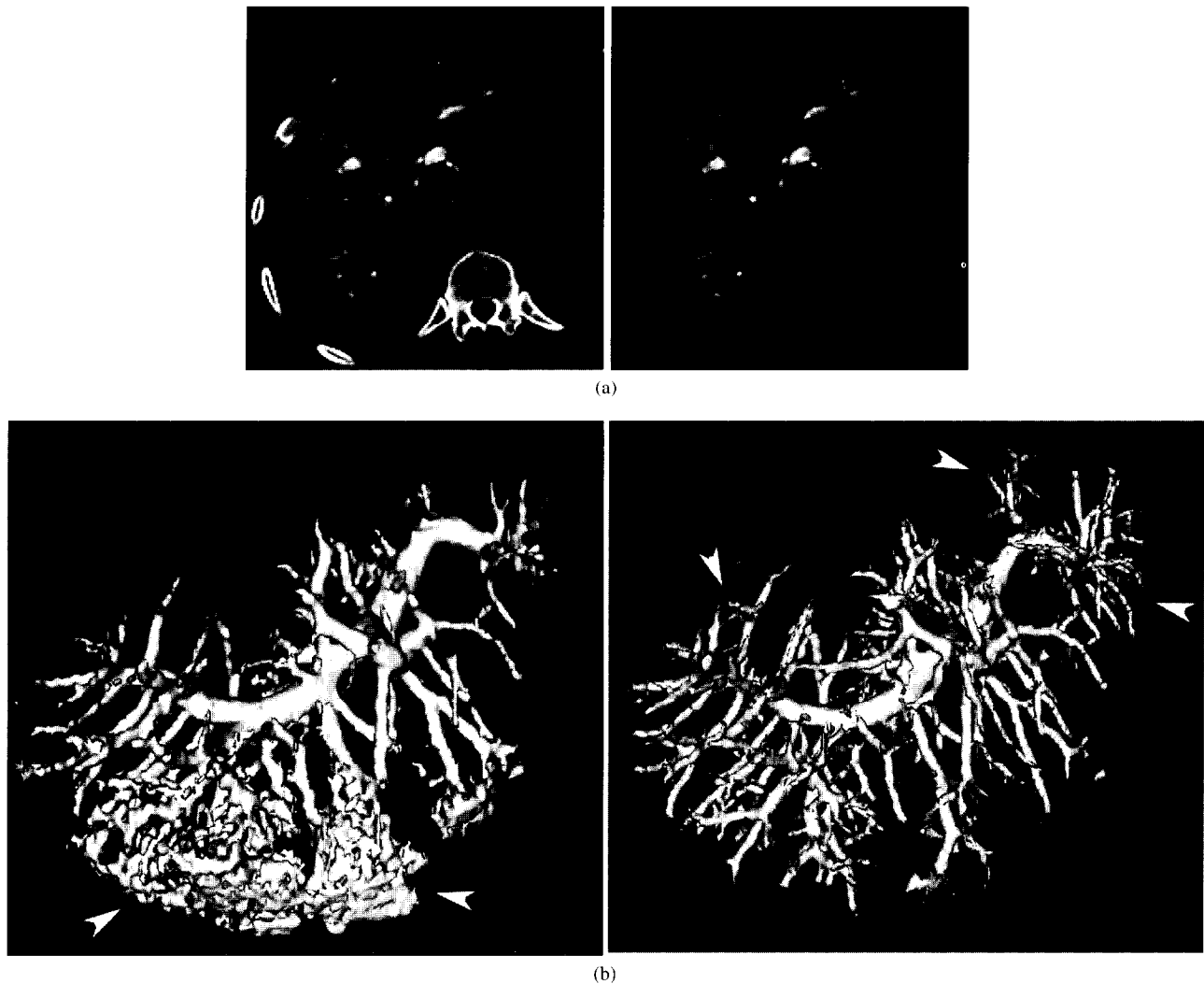


Figure 15. Liver vessel (portal vein) segmentation from abdominal CT images. (a) Input images. Left, original image (after intensity conversion); right, masked original image. (b) Surface rendering of segmented portal veins. Left, original images—small vessels appear buried due to the nonuniformity of the contrast material (indicated by arrowheads); right, combined images of original and line-filtered images—the nonuniformity of the contrast material is canceled out and the recovery of small vessels is significantly improved over the entire liver area (indicated by arrowheads).

6. DISCUSSION AND CONCLUSION

We have described a multi-scale 3-D line filtering method. The characteristics of the line filter were analyzed using the 3-D line model with a Gaussian cross section and other mathematical line models. The characteristics of multi-scale integration were also examined using the height and width measures of the filter responses in order to derive the criteria for scale sampling. We clarified how the height and width of original line structures can be preserved in a multi-scale response with discrete scales. In several experiments, we

showed that the quality of segmentation and visualization of curvilinear structures such as vessels and bronchi from 3-D medical images is significantly improved using the line filter.

Several image-enhancement methods designed to improve the delineation of vessels and reduce noise of 3-D MRA data have been proposed (Vandermeulen *et al.*, 1992; Du *et al.*, 1995a, b; Lock *et al.*, 1995). These methods can be classified into two approaches: orientation-sensitive smoothing (Vandermeulen *et al.*, 1992; Lock *et al.*, 1995) and directional second derivatives with adaptive orientation selection (Du *et al.*, 1995a, b). Our method is based on the directional

second derivatives of Gaussian-smoothed images using different scales with adaptive orientation selection using the Hessian matrix. As such, it can be viewed as a generalization of the latter approach. We tested several sets of MRA data and confirmed the improved continuity of vessel structures and noise reduction in all the cases. In MRA, however, the improvement was not as significant as in the experimental results for other modalities since the imaging method of MRA is itself suitable enough for the direct visualization of vessels without post-processing. In contrast to the MRA data, the role of the line filter was much more significant in the vessel visualization from MR images of the brain shown in Figure 13. Using the line filter, the direct visualization of vessels was possible without the need for any complex manual operations. We tested another two cases in which both MR and MRA images obtained from the same patient were available. The MRA was tuned with the velocity of the veins. In both cases, similar vein structures were observed in the volume-rendered images of the line-filtered MR images and the MRA images. In addition, the line filter was shown to be highly useful in bronchus and portal vein segmentation from CT images, both for the recovery of small structures and the removal of unwanted structures.

We have demonstrated the segmentation and visualization of vessels and bronchi in applications to their use as landmarks and road maps for image-guided surgery and biopsy. One of the main purposes of visualizing curvilinear structures in diagnostic imaging, however, is to detect and localize stenoses or aneurysms. As discussed in Section 3, with regard to stenoses, line filtering should be effective as long as the width of a stenotic part is included in the range within which the multi-scale integration behaves well. In the results shown in Subsection 5.2 (Figure 11c), the visualization of the stenotic part of the bronchus structure was clearer than in the original and conventional Gaussian-filtered images. The line filter would be useful as a means of initial visualization to locate stenoses and specify a region of interest where subsequent quantitative analysis of stenosis severity should be performed. However, our current segmentation method based on thresholding after line enhancement is not appropriate for quantification of stenosis severity because the line width in the resultant segmentation is quite sensitive to the threshold value. Although our line measure is based on a straightforward use of the eigenvalues of the Hessian matrix, a more elaborate formulation is needed to estimate line orientation, center position and the width for stenosis quantification. In the 2-D domain, we have already developed a method for quantification of stenosis severity, in which a threshold is not incorporated, from X-ray angiograms using an extension of the 2-D line filter based on the Hessian method (Sato *et al.*, 1998). We are now considering extending and modifying the

formulation of the multi-scale 3-D line filter to the 3-D quantification of stenosis severity. With respect to the aneurysms, our 3-D line filter is basically not intended to preserve the aneurysm shape. A different similarity measure needs to be defined for aneurysm detection so that it removes unwanted components such as noise and artefacts while aneurysm shape is preserved as much as possible.

In the experiments described in Subsections 5.2 and 5.4, we needed to convert the intensity level in order to obtain good performance of the line filter. Although the method is designed so as to enhance line structures, it does also give some response to other high-contrast structures, since it is based on second derivatives. To maximize the performance of line filtering, it is desirable to adjust the intensity range so as not to include other high-contrast structures. The necessity of such pre-processing is a drawback of the method. However, the intensity values of CT and MRI data are directly related to the imaged tissue or contrast material, and the intensity values do not vary greatly among different data sets. Thus, further parameter adjustment is unnecessary for different data sets imaged under similar imaging conditions once the appropriate range for conversion has been determined.

In previous work on 2-D line detection (Vandarbrug, 1975; Koller *et al.*, 1995), the problem of false detection at the edges has been addressed. In the experiment described in Subsection 5.3 (Figure 13), however, the line filter gave a high level of response at the rims of biopsy holes. To remove these false detections, this problem needs to be addressed in the 3-D domain. For this purpose, the non-linear combination of the first derivatives on both sides of a line has been used in 2-D line detection (Vandarbrug, 1975; Koller *et al.*, 1995). 2-D blob detection is also considered to be a sub-problem of 3-D line detection (Isobe *et al.*, 1993; Shimizu *et al.*, 1993; Yamamoto *et al.*, 1996). After the line direction in 3-D is determined, the problem of 3-D line detection is related to 2-D blob detection in the cross-sectional 2-D image orthogonal to the line direction. The minimum of directional second derivatives (MinDD) proposed for automatic nodule detection from X-ray images (Shimizu *et al.*, 1993) is based on a similar idea to λ_{\min_2} in Equation (10). Since the MinDD gives high responses to 2-D corners (which correspond to rims in 3-D) as well as blobs, a kernel with a quoit shape has been used to reduce false detections based on the analogy that a quoit does not fit a corner but a blob (Isobe *et al.*, 1993), and extended to 3-D blob detection (Yamamoto *et al.*, 1996). In future work, a method of removing false detections in 2-D blob and line detection may be combined with the similarity measure to a line in 3-D images.

In this paper, we have focused on the enhancement and discrimination of line structures. The method described in this paper can be naturally extended to deal with other local

intensity structures (Westin, 1994). Viewed from the point of view of tissue classification in 3-D medical images, we have found that the tissues of vessels and bronchi can be more reliably classified based on the similarity measure to a line than on the original intensity value. We are now generalizing the multi-scale 3-D filter for the enhancement of blob, sheet and edge structures so as to classify tissues using multi-dimensional space whose axes represent similarity measures to different local structures (Sato *et al.*, 1997c).

ACKNOWLEDGEMENTS

This work was partly supported by NIH grant P01 CA67165-02. The authors would like to thank Dr Don Johann of New York University Medical School for providing MR and DSA images of the brain, Dr Shinjiro Kawato of Mitsubishi Electric Corporation for providing the 3-D thinning program, and Dr Ahbir Bhalarao for making the volume rendering package 'VolPack' available at the Surgical Planning Laboratory, Harvard University and Brigham and Women's Hospital. The first author would also like to thank Dr Carl-Fredric Westin for encouraging him to use 3-D local intensity structures, Dr Nobuhiko Hata for helping him adapt the environment of the Surgical Planning Laboratory, and Professor Frank Jolesz of Harvard Medical School and Professor Shinichi Tamura of Osaka University Medical School for their continuous encouragement.

REFERENCES

- Burt, P. J. and Adelson, E. H. (1983) The Laplacian pyramid as a compact image code. *IEEE Trans. Commun.*, 31, 532–540.
- Du, Y. P., Parker, D. L., Davis, W. L. and Cao, G. (1994) Reduction of partial-volume artifacts with zero-filled interpolation in three-dimensional MR angiography. *J. Magn. Reson. Imag.*, 4, 733–741.
- Du, Y. P., Parker, D. L. and Davis, W. L. (1995) Vessel enhancement filtering in three-dimensional MR angiography. *J. Magn. Reson. Imag.*, 5, 151–157.
- Dumoulin, C. L., Souza, S. P., Walker, M. F. and Wagle, W. (1989) Three-dimensional phase contrast angiography. *Magn. Reson. Med.*, 9, 139–149.
- Edelman, R. R., Mattle, H. P., Atkinson, D. J. and Hoogewoud, H. M. (1990) MR angiography. *AJR Am. J. Roentgenol.*, 154, 937–946.
- Fischler, M., Tenenbaum, J. and Wolf, H. (1981) Detection of roads and linear structures in low-resolution aerial imagery using a multi source knowledge integration. *Comput. Graphics Image Process.*, 15, 201–223.
- Gauch, J. M. and Pizer, S. M. (1993) Multiresolution analysis of ridges and valleys in grey-scale images. *IEEE Trans. PAMI*, 15, 635–646.
- Goodenough, D. J., Rossmann, K. and Lusted, L. B. (1974) Radiographic applications of receiver operating characteristics (ROC) curves. *Radiology*, 110, 89–95.
- Haralick, R. M., Watson, L. T. and Laffey, T. J. (1983) The topographic primal sketch. *Int. J. Robotic Res.*, 2, 50–72.
- Hylton, N. M., Simovsky, I., Li, A. J. and Hale, J. D. (1992) Impact of section doubling on MR angiography. *Radiology*, 185, 899–902.
- Isobe, Y., Ohkubo, N., Yamamoto, S., Toriwaki, J. and Kobatake, H. (1993) Characteristics of quoit filter, a digital filter developed for the extraction of circumscribed shadows, and its application to mammograms. *IEICE Trans.*, J-76D-II, 279–287.
- Kikinis, R. *et al.* (1996) Computer-assisted interactive three-dimensional planning for neurosurgical procedures. *Neurosurgery*, 38, 640–651.
- Kitamura, K., Tobis, J. M. and Sklansky, J. (1989) Estimating the 3-D skeletons and transverse areas of coronary arteries from biplane angiograms. *IEEE Trans. Med. Imag.*, 7, 173–187.
- Koller, T. M., Gerig, G., Szekely, G. and Dettwiler, D. (1995) Multi-scale detection of curvilinear structures in 2-D and 3-D image data. In *Proc. 5th Int. Conf. Computer Vision*, Boston, MA, pp. 864–869. IEEE.
- Lacroute, P. and Levoy, M. (1994) Fast volume rendering using a shear-warp factorization of the viewing transform. In *Proc. SIGGRAPH'94*, pp. 451–458. (The VolPack volume rendering library, at <http://www-graphics.stanford.edu/software/volpack> (1994) Stanford, CA, USA.)
- Levoy, M. (1988) Display of surfaces from volume data. *IEEE Comp. Graphics Appl.*, 8, 29–37.
- Lewis, B. and Berg, D. J. (1996) *Threads Primer: a Guide to Multithreaded Programming*. Prentice-Hall, Upper Saddle River, NJ.
- Lindeberg, T. (1996) Edge detection and ridge detection with automatic scale selection. In *Proc. IEEE Computer Society Conf. on Computer Vision and Pattern Recognition (CVPR'96)*, pp. 465–470.
- Lock, T., Westin, C.-F., Haglund, L., Wigström, L., Sjökvist, L. and Knutsson, H. (1995) Multidimensional adaptive filtering of MRA data. In *Proc. Society of Magnetic Resonance and European Society for Magnetic Resonance in Medicine and Biology Joint Meeting*, Nice, France.
- Lorenz, C., Carlsen, I.-C., Buzug, T. M., Fassnacht, C. and Wesse, J. (1997) Multi-scale line segmentation with automatic estimation of width, contrast and tangential direction in 2D and 3D medical images. In *Proc. 1st Joint Conf. CVRMed and MRCAS (CVRMed/MRCAS'97)*, pp. 233–242.
- Mori, K., Hasegawa, J., Toriwaki, J., Anno, H. and Kagada, K. (1995) Automated extraction and visualization of bronchus from 3D CT images of lung. In *Proc. 1st Int. Conf. on Computer Vision, Virtual Reality, and Robotics in Medicine (CVRMed'95)*, pp. 549–554.
- Nakajima, S., Atsumi, H., Kikinis, R., Moriarty, T. M., Metcalf, D. C., Jolesz, F. A. and Black, P. McL. (1997) Use of cortical surface vessel registration for image-guided neurosurgery. *Neurosurgery*, 40, 1201–1210.

- Prince, M. R., Yucel, E. K., Kaufmann, J. A., Harrison, D. C. and Geller, S. C. (1993) Dynamic gadolinium-enhanced three-dimensional abdominal MR arteriography. *J. Magn. Reson. Imag.*, 3, 877–881.
- Rosenfeld, A. and Thurston, M. (1971) Edge and curve detection for visual scene analysis. *IEEE Trans. Computer*, 20, 562–569.
- Rougée, A., Picard, C., Saint-Félix, D., Trouset, Y., Moll, T. and Amie, M. (1994) Three-dimensional coronary arteriography. *Int. J. Cardiac Imag.*, 10, 67–70.
- Sato, Y., Chen, J., Harada, N., Tamura, S. and Shiga, T. (1997a) Automatic extraction and measurement of leukocyte motion in microvessels using spatiotemporal image analysis. *IEEE Trans. Biomed. Engng*, 44, 225–236.
- Sato, Y., Nakajima, S., Atsumi, H., Koller, T., Gerig, G., Yoshida, S. and Kikinis, R. (1997b) 3D multi-scale line filter for segmentation and visualization of curvilinear structures in medical images. In *Proc. 1st Joint Conf. on CVRMed and MRCAS (CVRMed/MRCAS'97)*, pp. 213–222.
- Sato, Y., Westin, C.-F., Bhalerao, A., Nakajima, S., Shiraga, N., Yoshida, S., Zientara, G. and Kikinis, R. (1997c) Tissue classification based on 3D local intensity structures for volume rendering. In *Proc. JAMIT Frontier '97*, Suita, Japan, pp. 167–172.
- Sato, Y., Araki, T., Hanayama, M., Naito, H. and Tamura, S. (1998) A viewpoint determination system for stenosis diagnosis and quantification in coronary angiographic image acquisition. *IEEE Trans. Med. Imag.*, 17, in press.
- Schroeder, W., Martin, K. and Lorensen, B. (1996) *The Visualization Toolkit: an Object-oriented Approach to 3D Graphics*. Prentice-Hall, Upper Saddle River, NJ.
- Shimizu, A., Hasegawa, J. and Toriwaki, J. (1993) Minimum directional difference filter for extraction of circumscribed shadows in chest X-ray images and its characteristics. *IEICE Trans.*, J-76D-II, 241–249.
- Vandarbrug, S. J. (1975) Serrilinear line detectors. *Comput. Graphics Image Process.*, 4, 287–293.
- Vandermeulen, D., Delaere, D., Suetens, P., Bosmans, H. and Marchal, G. (1992) Local filtering and global optimisation methods for 3D magnetic resonance angiography (MRA) image enhancement. In *Proc. Visualization in Biomedical Computing (VBC'92)*, pp. 274–288.
- Westin, C.-F. (1994) *A Tensor Framework for Multidimensional Signal Processing*. Thesis No 348, ISBN 91-7871-421-4, Linköping University, Sweden.
- Yamamoto, S., Matsumoto, M., Tateno, Y., Iinuma, T. and Matsumoto, T. (1996) Quoit filter: a new filter based on mathematical morphology to extract the isolated shadow, and its application to automatic detection of lung cancer in X-ray CT. In *Proc. 13th Int. Conf. Pattern Recognition (ICPR'96)*, pp. 2, 3–7.

APPENDICES

A. MATHEMATICAL LINE MODELS

A.1 Curved line model

The curved line model which we used is given by

$$L_{\text{curve}}(\mathbf{x}; \sigma_r, r) = \exp\left\{-\frac{x'^2 + y'^2}{2\sigma_r^2}\right\}, \quad (\text{A1})$$

where

$$x' = \begin{cases} x - z - \sqrt{2}r, & t > \pi/4 \\ \sqrt{(x - r \cos t)^2 + (z - r \sin t)^2}, & |t| \leq \pi/4 \\ x + z + \sqrt{2}r, & t < -\pi/4 \end{cases} \quad (\text{A2})$$

in which

$$t = \arctan \frac{z}{x}. \quad (\text{A3})$$

The center line of this model represents a corner with a right angle. The radius of curvature of the corner is r . We synthesized curved lines with different values of normalized curvature κ ($= \sigma_r/r$) by changing σ_r and r in this model. In the simulation shown in Figure 4a, we used $\sigma_r = 1.5$.

A.2 Curved line with low-intensity line

$L_{\text{curve}}(\mathbf{x}; \sigma_r, r)$ [in Equation (A1)] and rotated and translated version of $t L(\mathbf{x}; \sigma_r)$ are combined to model a curved line with a low-intensity line, where $L(\mathbf{x}; \sigma_r)$ is an ideal bright line shown in Equation (6) and $t < 1$. To make the intensity of the straight line sufficiently low, we set t much smaller than one. In the simulation shown in Figure 4b, we used $t = 0.05$, $\sigma_r = 1.5$ and $r = 6$ (that is, $\kappa = \sigma_r/r = 0.25$), Gaussian noise with a standard deviation of 0.0375 was added.

A.3 Branch model

The branch model which we used is given by

$$L_{\text{branch}}(\mathbf{x}; \sigma_r) = \begin{cases} L(\mathbf{x}; \sigma_r), & x < 0 \\ \max\left\{L(\mathbf{x}; \sigma_r), \exp\left(-\frac{y^2 + z^2}{2\sigma_r^2}\right)\right\}, & x \geq 0 \end{cases} \quad (\text{A4})$$

In the simulation shown in Figure 5, we used $\sigma_r = 1$. In Figure 5a–d, Gaussian noise with standard deviation 0.3 was added. In the result shown in Figure 5e, Gaussian noise was not added.

B. NORMALIZED LINE FILTER RESPONSE TO IDEAL LINE

The normalized line filter response to an ideal line is given by

$$R_L(\mathbf{x}; \sigma_r, \sigma_l) = \sigma_l^2 \left\{ -\frac{\partial^2}{\partial x^2} G(\mathbf{x}; \sigma_l) \right\} * L(\mathbf{x}; \sigma_r). \quad (\text{B1})$$

Since $L(\mathbf{x}; \sigma_r)$ is a function of only x and y , Equation (B1) is equivalent to

$$R_L(\mathbf{x}; \sigma_r, \sigma_f) = \sigma_f^2 \left\{ -\frac{\partial^2}{\partial x^2} G(x, y; \sigma_f) \right\} * \exp\left(-\frac{x^2 + y^2}{2\sigma_r^2}\right), \quad (\text{B2})$$

where $G(x, y; \sigma)$ is a 2-D isotropic Gaussian function with standard deviation σ . $\exp[-(x^2 + y^2)/2\sigma_r^2]$ can be rewritten as

$$\exp\left(-\frac{x^2 + y^2}{2\sigma_r^2}\right) = (\sqrt{2\pi}\sigma_r)^2 G(x, y; \sigma_r). \quad (\text{B3})$$

By combining Equations (B2) and (B3), we have

$$\begin{aligned} R_L(\mathbf{x}; \sigma_r, \sigma_f) &= \sigma_f^2 (\sqrt{2\pi}\sigma_r)^2 \left\{ -\frac{\partial^2}{\partial x^2} G(x, y; \sigma_f) * G(x, y; \sigma_r) \right\} \\ &= \sigma_f^2 (\sqrt{2\pi}\sigma_r)^2 \left\{ -\frac{\partial^2}{\partial x^2} G(x, y; \sqrt{\sigma_f^2 + \sigma_r^2}) \right\}, \quad (\text{B4}) \end{aligned}$$

where we used the relation $G(x, y; \sigma_1) * G(x, y; \sigma_2) = G(x, y; \sqrt{\sigma_1^2 + \sigma_2^2})$. Since

$$\begin{aligned} \frac{\partial^2}{\partial x^2} G(x, y; \sigma) &= \left\{ \frac{x^2 - \sigma^2}{\sqrt{2\pi}\sigma^5} \exp\left(-\frac{x^2}{2\sigma^2}\right) \right\} \\ &\quad \times \left\{ \frac{1}{\sqrt{2\pi}\sigma} \exp\left(-\frac{y^2}{2\sigma^2}\right) \right\}, \quad (\text{B5}) \end{aligned}$$

we have

$$R_L(0, 0, z; \sigma_r, \sigma_f) = \frac{\sigma_f^2 \sigma_r^2}{(\sqrt{\sigma_f^2 + \sigma_r^2})^4}. \quad (\text{B6})$$

Especially when $\sigma_f = \sigma_r$, $R_L(0, 0, z; \sigma_r, \sigma_f) = \frac{1}{4}$.

C. CONTENT OF THE VIDEO

The video consists of three sequences:

- (i) Original MR images shown in the left-hand frame of Figure 13a.
- (ii) Volume-rendered images of the original MR images shown in the left-hand frame of Figure 13b.
- (iii) Volume-rendered images of the line-filtered MR images shown in the right-hand frame of Figure 13b.



知网查重限时 7折 最高可优惠 120元

本科定稿，硕博定稿，查重结果与学校一致

立即检测

免费论文查重: <http://www.paperyy.com>

3亿免费文献下载: <http://www.ixueshu.com>

超值论文自动降重: http://www.paperyy.com/reduce_repetition

PPT免费模版下载: <http://ppt.ixueshu.com>
